Original Paper

Stochastic seismic inversion and Bayesian facies classification applied to porosity modeling and igneous rock identification

Fábio Júnior Damasceno Fernandes [a, *], Leonardo Teixeira [a, b],
Antonio Fernando Menezes Freire [a, c], Wagner Moreira Lupinacci [a, c]

[a] *Exploratory Interpretation and Reservoir Characterization Group (GIECAR), Department of Geology and Geophysics, Federal Fluminense University, Niterói, RJ, 24210-346, Brazil*
[b] *Petrobras, Rio de Janeiro, RJ, 20231-030, Brazil*
[c] *National Institute of Science and Technology of Petroleum Geophysics (INCT-GP/CNPQ), Niterói, RJ, 24210-346, Brazil*

ARTICLE INFO

ABSTRACT

We apply stochastic seismic inversion and Bayesian facies classification for porosity modeling and igneous rock identification in the presalt interval of the Santos Basin. This integration of seismic and well-derived information enhances reservoir characterization. Stochastic inversion and Bayesian classification are powerful tools because they permit addressing the uncertainties in the model. We used the ES-MDA algorithm to achieve the realizations equivalent to the percentiles P10, P50, and P90 of acoustic impedance, a novel method for acoustic inversion in presalt. The facies were divided into five: reservoir 1, reservoir 2, tight carbonates, clayey rocks, and igneous rocks. To deal with the overlaps in acoustic impedance values of facies, we included geological information using *a priori* probability, indicating that structural highs are reservoir-dominated. To illustrate our approach, we conducted porosity modeling using facies-related rock-physics models for rock-physics inversion in an area with a well drilled in a coquina bank and evaluated the thickness and extension of an igneous intrusion near the carbonate-salt interface. The modeled porosity and the classified seismic facies are in good agreement with the ones observed in the wells. Notably, the coquinas bank presents an improvement in the porosity towards the top. The *a priori* probability model was crucial for limiting the clayey rocks to the structural lows. In Well B, the hit rate of the igneous rock in the three scenarios is higher than 60%, showing an excellent thickness-prediction capability.

1. Introduction

Quantitative seismic interpretation combines several methods for estimating three-dimensional models of elastic parameters and petrophysical properties in the subsurface based on the integration of geophysical, geological, and reservoir engineering data. The routines include seismic data pre-conditioning, seismic attributes, seismic inversion, rock physics, facies and petrophysical properties modeling, geostatistics, well-logs upscale, and 4D seismic (Avseth et al., 2005; Dvorkin et al., 2014; Simm and Bacon, 2014). More recently, machine learning and deep learning algorithms have been employed in quantitative seismic interpretation (Braga et al., 2019;

Allo et al., 2021; Vizeu et al., 2021). The goals of using all these methods are the evaluation of uncertainty in the model and the risk reduction during petroleum exploration and production. The uncertainties associated with the model can be evaluated through probability distributions, confidence intervals, or a set of model realizations (Grana et al., 2021).

In recent years, several studies employed quantitative seismic interpretation methods in Brazilian presalt carbonates for potential reservoirs identification (Dias et al., 2019; Peçanha et al., 2019; Barnett et al., 2021; Ferreira et al., 2021; Penna and Lupinacci, 2021), porosity forecasting (Teixeira et al., 2017), igneous rocks identification (Penna et al., 2019; Vizeu et al., 2021), gas-oil ratio predictions (Oliveira et al., 2018), seismic features identification and characterization (Jesus et al., 2019), and injector wells location (Cunha et al., 2019). Although all these studies integrate different quantitative seismic interpretation tools, each methodology is

unique. This highlights that there is no single or best way to perform the quantitative seismic interpretation. An adequate methodology has to be selected considering the different challenges encountered in the study area, the available data, and their quality (Gonzalez et al., 2016).

Seismic inversion is a routine in quantitative seismic interpretation and reservoir characterization that promotes the passage from an interface attribute (seismic amplitude) to a layer property (acoustic impedance). Hence, seismic inversion helps the interpretation and quantification of reservoir properties and their spatial distribution (Latimer, 2011). Seismic inversion methods can be divided into deterministic and stochastic techniques. An advantage of the stochastic methods is the uncertainty quantification. Currently, there are several methods for performing stochastic seismic inversion, such as Bayesian analytical inversion (Buland and Omre, 2003; Tarantola, 2005), Monte Carlo methods (Bortoli et al., 1993; Connolly and Hughes, 2016), stochastic optimization algorithms (Liu and Grana, 2018, 2019; Cyz and Azevedo, 2020), and probabilistic deep learning (Das et al., 2019; Bhattacharya, 2021). Grana et al. (2022) provided an overview of some of the most recent research advances and classical algorithms in stochastic seismic inversion and joint seismic rock-physics inversion. The method that Liu and Grana (2018) applied to stochastic inversion is called ensemble smoother with multiple data assimilation (ES-MDA). This is an ensemble-based data-assimilation algorithm commonly used in reservoir engineering for history matching (Emerick and Reynolds, 2013; Canchumuni et al., 2019). Liu and Grana (2018) were the first to employ it for seismic inversion. In the ES-MDA, the data assimilations iteratively update the prior distribution by approximating the conditional distribution of the model parameters with the empirical mean and covariances of the ensemble members. Thus, the posterior distribution represents the model conditioned by data assimilations. ES-MDA implementation is reasonably simple and has an acceptable computational cost for many applications, as is the case of seismic inversion. Although Liu and Grana (2018) proposed the ES-MDA application for stochastic elastic inversion, its extension can be easily adapted for stochastic acoustic inversion. This algorithm has not yet been used for seismic inversion in the presalt.

Facies classification on seismic volume can be achieved in a one-step to a multi-step approach. One-step approaches represent the direction inference of facies using seismic data, as seismic facies inversion (Grana et al., 2012, 2021; Lang and Grana, 2017; Kolbjørnsen et al., 2020) and deep learning for classification (Vizeu et al., 2021). Two-step methods use elastic parameters from seismic inversion and/or seismic attributes as input for clustering and pattern recognition algorithms and Bayesian classification (Mukerji et al., 2001; Ferreira et al., 2021). Multi-step approaches can integrate some of these methods for fine-tuning the facies model. Mukerji et al. (2001) disseminated "statistical rock physics" methods, a two-step method, for facies classification from elastic properties using Bayes' theorem. In this approach, the facies are pointwise classified through the relationship between elastic parameter(s) and facies, integrating the elastic parameter(s) with something directly related to reservoir properties, which are the facies. The Bayesian classification is a powerful method due to the capability of uncertainty estimation and combining petrology and geology in the definition of facies (Gonzalez et al., 2016). Recent papers used this methodology to understand the facies distribution in the presalt interval (Teixeira et al., 2017; Oliveira et al., 2018; Penna et al., 2019; Penna and Lupinacci, 2021; Lebre et al., 2021; Mello and Lupinacci, 2022).

As in seismic facies classification, petrophysical properties modeling can also be achieved by a one-step to a multi-step strategy. Joint seismic rock-physics inversion refers to the estimation of petrophysical properties from seismic data based on rock-physics relations, while the two-step method consists of the seismic petrophysical properties calculation by rock-physics inversion using the elastic inverted volume(s) (Grana et al., 2022). In the three-step approach, classified facies can be used as a constraint with the inverted volume(s) for rock-physics inversion. Establishing empirical relationships between porosity and acoustic impedance conditioned by facies is a simple and efficient way to perform the porosity modeling after stochastic acoustic inversion and facies inference in a three-step manner. In the presalt interval, Penna and Lupinacci (2021) successfully used empirical relationships between these two variables for petrophysical property modeling using lithofacies and flow units as a constraint.

Some of the main presalt reservoirs are interpreted in seismic features like carbonate platforms, mounds, and coquina banks (Carlotto et al., 2017; Jesus et al., 2019; Ferreira et al., 2021). Identifying good reservoir intervals in these seismic structures is challenging due to several factors. An example is the overlap of acoustic impedance values of porous carbonates and clayey facies (Teixeira et al., 2017). The presence of intrusive and extrusive igneous rocks in the presalt is also a feature that complicates quantitative seismic interpretation and reservoir characterization. In areas with igneous rock presence, an overlap of the acoustic impedance values of igneous with the low-porosity carbonates is observed (Penna et al., 2019). Elastic parameters such as shear impedance and the ratio between P-wave velocity and S-wave velocity tend to reduce the uncertainty of facies in presalt reservoirs. Recent studies discuss models and approaches for identifying these igneous bodies throughout well-log (Oliveira et al., 2019) and seismic data (Penna et al., 2019; Ren et al., 2019; Zhao et al., 2019; Vizeu et al., 2021). Intrusive igneous bodies typically occur near the salt-carbonate interface concordant with the layers, whereas the dominant occurrence of extrusive igneous rocks prevails near the base of the Itapema Formation (Penna et al., 2019).

We apply quantitative seismic interpretation routines for the porosity modeling of an interval with a well drilled in a coquina bank and to map the extension and thickness of an igneous rock intrusion in a presalt field. Our workflow consists of a three-step approach: stochastic acoustic inversion, Bayesian classification, and porosity modeling. The first step is to use the ES-MDA algorithm to perform stochastic acoustic inversion. With the acoustic impedance realizations equivalent to the percentiles P10, P50, and P90, we perform Bayesian facies classification to estimate the probability of the facies: reservoir 1 (high-porosity carbonates), reservoir 2 (intermediate-porosity carbonates), tight carbonates (low-porosity carbonates), clayey rocks, and igneous rocks by including a prior geological knowledge to update the *a posteriori* probability of these facies. Finally, we model the seismic-driven porosity by applying the well-log-based, facies-dependent empirical relationships between porosity and acoustic impedance. For the area of the well drilled in the coquina bank, we explore the three steps of the workflow, while for the igneous intrusion area, we evaluate the stochastic acoustic inversion and Bayesian classification exclusively.

2. Study area and dataset

Santos Basin is located in the southeastern Brazilian margin, with an area of approximately 350,000 km^2. The basin is limited to the south by the Florianopolis High and to the north by the Cabo Frio High, with its reservoirs representing 74.7% of Brazilian petroleum production during 2022 (ANP, 2022). Santos Basin is a distension-margin basin that has its origin associated with the breakup of the supercontinent Gondwana and the formation of the South Atlantic Ocean (Milani et al., 2007). The presalt carbonate

reservoirs were developed in a lacustrine environment, with unique features that are very different from the ones observed in conventional lake deposits and classic marine carbonates, representing a challenge for its characterization (Wright and Barnett, 2015; Herlinger et al., 2017).

The presalt reservoirs comprise the coquinas from the Itapema Formation (Neobarremian-Eoaptian) and the carbonates from the Barra Velha Formation (Aptian). The coquinas of the Itapema Formation are interpreted as bivalves rudstones, grainstones, floatstones, packstones, and wackestones, which were deposited in the rift phase of the basin (Chinelatto et al., 2020). The structural lows present non-reservoir low-energy facies like black shales rich in organic matter. The lower limit of the Itapema Formation is the Pre-Jiquiá Unconformity, and the upper limit is the Pre-Alagoas Unconformity, which represents the transition to the Barra Velha Formation (Moreira et al., 2007; Pietzsch et al., 2018). According to Oliveira et al. (2021), the coquinas were deposited in a period of continuous accommodation space generation and high carbonate production rate. This process culminated in a sedimentary record characterized by sigmoidal clinoforms in a retrogradational context, producing the aspect of banks on the coquinas deposits.

In Barra Velha Formation, the main reservoir facies are shrubs and spherulites deposited in a shallow, evaporitic, and hyperalkaline lacustrine carbonate platform (Wright and Rodriguez, 2018). The lower interval of the Barra Velha Formation was deposited during the upper rift phase, with the Intra-Alagoas Unconformity marking the passage to the sag phase. However, this unconformity is sometimes hard to track on seismic data. The Barra Velha Formation ends up with the salt deposition of the Ariri Formation, marked by the seismic horizon called Base of Salt. The facies found in the formation are formed by three main in-situ components: calcite shrubs, spherulites, and mud (Wright and Barnett, 2015). Some of the seismic patterns characterized in the Barra Velha Formation are mounds, carbonate platforms, debris, and bottom-lake deposits (Wright and Rodriguez, 2018; Neves et al., 2019; Ferreira et al., 2021).

Igneous rocks are characteristic in some areas of the presalt of the Santos Basin (Oliveira et al., 2019; Penna et al., 2019; Ren et al., 2019; Zhao et al., 2019). Moreira et al. (2007) identified four major magmatic events that affected the basin: Valanginian-Hauterivian, Aptian, Santonian-Campanian, and Eocene. The events of Valanginian-Hauterivian and Aptian are associated with the presence of extrusive rocks in presalt, like the Early Aptian basalt in the Itapema Formation and the Late Aptian basalt in the Barra Velha Formation. On the other hand, the events of Santonian-Campanian and Eocene developed more intrusive rocks in the presalt, and both intrusive and extrusive in the post-salt interval. Regarding the composition, these igneous rocks are majorly basic according to their silica content (Ren et al., 2019). Zhao et al. (2019) proposed that the faults play a key role in these magmatic events, working as a conduit for magma migration. Thus, two major effects associated with the presence of igneous rocks affect the presalt carbonates: contact metamorphism and hydrothermalism (Ren et al., 2019). In this case, the contact metamorphism of the igneous rock impacts the carbonate reservoirs with a decrease in porosity by promoting recrystallization. The general consequence of the percolation of the hydrothermal fluid is also porosity reduction due to factors like silicification and dolomitization.

The dataset available for this work comprises nine wells and a 3D prestack depth-migrated (PSDM) seismic volume with a bin-size of 25 m × 25 m, the sample rate of 5 m, zero phase, and SEG Polarity from a presalt field in the Santos Basin, Brazil. The company used the reverse time migration (RTM) and tilted transverse isotropy (TTI) velocity model for the migration. The peak frequency of the seismic data in the presalt interval is 16.8 Hz. Due to data confidentiality, it is not possible to show explicit details about seismic, the wells names and depths, and the location of the study area. The results will be evaluated using seismic sections crossing two wells, called Well A and Well B.

3. Theory

3.1. Seismic inversion

Seismic inversion is a valuable tool for seismic reservoir characterization as it promotes the transformation from the seismic amplitude data to the elastic properties of layers. It is based on the inverse theory, a field of mathematics for estimating the model variables from the observed data by assuming physical relations between the data and model (Tarantola, 2005). In the elastic seismic inversion, the relationship between the model and data is given by the nonlinear and angle-dependent set of Zoeppritz equations, as well as by their linear approximations (Aki and Richards, 1980; Shuey, 1985; Fatti et al., 1994). It yields more than one elastic property, such as P-wave velocity, S-wave velocity, and density. The seismic acoustic inversion, or seismic impedance inversion, is based on the convolution between a wavelet and the reflectivity series, given by the acoustic impedance contrasts. This relation is independent of the acquisition angle, and the parameter recovered in the inversion process is the acoustic impedance.

Aster et al. (2004) and Tarantola (2005) are classical references that provide complete foundations and several applications of seismic impedance inversion. Russell (1988) visited some of the first methods applied for seismic inversion, such as recursive inversion and model-based inversion. Wang (2016) focused on the practical aspects of different seismic inversion methods, introducing a new wave equation-based inversion approach. Simm and Bacon (2014) gave an overview of the inversion process and discuss some inversion issues found in seismic reservoir characterization.

Seismic inversion is a deconvolution problem relating the reflection coefficients to the observed seismic data. The reflection coefficients represent the response of subsurface geology to the contrasts of acoustic impedance between rocks. In the continuous form, the acoustic impedance $z(t)$ can be considered as a function of time t. Considering a weak-contrast medium with $r(t) < 0.3$, which is usually the case, the reflectivity series $r(t)$ is approximately expressed as (Russell, 1988)

$$r(t) = \frac{1}{2} \frac{d(\ln(z(t)))}{dt}. \tag{1}$$

Discretizing Eq. (1) on a uniform finite-difference grid, it can be written as

$$\mathbf{r} = \mathbf{D}_t \mathbf{m}, \tag{2}$$

where $\mathbf{r} = [r_1, r_2, ..., r_{N-1}]^T$ is the reflectivity series, in which N is the number of samples in an acoustic impedance trace; $\mathbf{D}_t$ is a first-order derivative matrix; and $\mathbf{m} = \frac{1}{2}[\ln(z_1), \ln(z_2), ..., \ln(z_N)]^T$. Thus, a seismic trace is written in the discrete form as

$$\mathbf{d} = \mathbf{W}\mathbf{D}_t \mathbf{m}, \tag{3}$$

where $\mathbf{W}$ is the wavelet convolution matrix. By renaming $\mathbf{G} = \mathbf{W}\mathbf{D}_t$ and adding a random noise $\mathbf{n}$ with the same frequency bandwith than $\mathbf{d}$, the forward modeling is

$$\mathbf{d} = \mathbf{G}\mathbf{m} + \mathbf{n}. \tag{4}$$

Eq. (4) defines the seismic forward modeling, specifically, the convolutional model as a linear problem. Zoeppritz equations are

an example where forward modeling is a nonlinear problem (Aki and Richards, 1980). Seismic impedance inversion consists of the estimation of the model parameter **m** given a seismic trace **d** and a known mapping operator **G**. An approximation for the inverse problem is finding a particular solution **m** that minimizes the difference between the observed and modeled data given some matching criterion. The minimization of this residual vector **r** is written as

$$\mathbf{r} = \mathbf{d} - \mathbf{Gm}. \tag{5}$$

Hence, seismic acoustic inversion is an optimization problem, and several algorithms can be used to minimize a cost function defined from the residual vector. However, seismic inversion problems are non linear, ill-conditioned, and nonunique due to the limitations of the seismic method, such as limited bandwidth and resolution of seismic reflection data, noisy nature of data, measurement errors, numerical approximations, and physical assumptions in the forward models (Tarantola, 2005; Azevedo and Soares, 2017). Thus, the acoustic model retrieved at the end of a seismic inverse process is just one result among several models that satisfy the observed seismic data. This nature of the seismic inversion problem asserts the necessity of estimating the uncertainty in the inverted models by accessing more than one model. Azevedo and Soares (2017) divide the seismic inversion approaches into deterministic and stochastic (probabilistic) frameworks. While deterministic inversion obtains a unique solution, the stochastic methods describe potential variabilities of the inverse solution using several realizations of the subsurface model, allowing uncertainty quantification.

Stochastic seismic inversion algorithms can be divided into two main groups: the methods that treat stochastic inversion as an optimization problem and the Bayesian linearized method (Azevedo and Soares, 2017). The first group approaches seismic inversion in an iterative process that converges the modeled data with the observed data. Within this group is the iterative geostatistical inversion presented by Bortoli et al. (1993). This method used sequential stochastic simulation algorithms to generate random, spatially-correlated acoustic impedance models. Its main limitation is that it is applied trace-by-trace, which makes it impossible to distinguish between signal and noise (Azevedo and Soares, 2017). Soares et al. (2007) introduced the global geostatistical inversion to overcome the limitations encountered in trace-by-trace approaches, using a global approach during the stochastic sequential simulation step. Alternative approaches were proposed for stochastic inversion, in which the results are facies, rock properties, and elastic parameter volumes (Grana et al., 2012; Lang and Grana, 2017). In recent decades, geostatistical inversion methods have been widely employed for predicting subsurface properties from seismic reflection data and assessing the uncertainties (Azevedo et al., 2019; Liu and Grana, 2019; Ketteb et al., 2019; Cyz and Azevedo, 2020).

The second group is called the linearized Bayesian inversion. This seismic inversion approach is based on a particular solution of Bayes' theorem. This solution assumes that the parameters, observations, and measurement errors are Gaussian distributed, linearizing the forward modeling (Buland and Omre, 2003; Tarantola, 2005). Gaussian mixture models emerged recently to overcome some limitations of this method, like the multi-Gaussian assumption (Grana and Della Rossa, 2010). The linearization of forward seismic modeling in the Bayesian framework achieves good approximations of the subsurface geophysical response for near-acquisition angles for the solution of the elastic properties (Aki and Richards, 1980). However, the solutions are highly nonlinear for the largest angles and in the rock-physics domain.

Since there is no analytical solution for nonlinear inverse problems, numerical methods must be adopted. Ensemble-based methods are used in these scenarios because they can handle the nonlinearity of the forward problem (Liu and Grana, 2018). The ensemble implicitly linearizes the relation between the parameters and the observed data working on finding a tangent linear model at each assimilation step using the ensemble. An ensemble corresponds to multiple realizations of a subsurface model and represents a random sample set from a probability distribution (Gineste et al., 2020). Grana et al. (2022) summarized the ensemble-based methods in the family of stochastic optimization algorithms.

ES-MDA is part of the ensemble-based data-assimilation methods based on the Kalman filter (Kalman, 1960). In the last three decades, ensemble-based methods have been widely employed for data assimilation in reservoir history-matching flow (Emerick and Reynolds, 2013; Canchumuni et al., 2019). These methods are data-assimilation algorithms in which the probability distribution of model parameters is represented by an ensemble of model realizations obtained from data assimilation. In the ensemble-based methods, the prior distribution of the model parameters and the distribution of observation errors are assumed to be Gaussian. Each data-assimilation step corresponds to a Bayesian update step in which the conditional distributions of the model parameters are approximated from the estimated conditional mean and covariance matrix of the ensemble members. Thus, a large number of ensemble members is required for the approximation to have reasonable accuracy. From this, the model parameters are considered approximately normal, and the forward modeling is not highly nonlinear (Liu and Grana, 2018). Using Gaussian prior and ensemble linearization implies that the posterior solution will be unimodal. Gaussian mixture models have been explored recently to impose multimodality in the posterior solution and to accommodate the effect of nonlinearity (Stordal, 2015). The first applications of ensemble-based methods for solving geophysical inverse problems were performed for full-waveform inversion (Gineste and Eidsvik, 2017; Thurin et al., 2017). After that, Liu and Grana (2018) proposed a joint seismic and rock-physics inversion method based on the ES-MDA.

The theoretical development of ES-MDA is based on the Kalman filter. In the Bayesian framework, the Kalman filter represents the maximum *a posteriori* (MAP) of the posterior distribution under Gaussian assumptions. The posterior probability distribution $f(\mathbf{m}|\mathbf{d})$ is conditioned by the prior distribution $f(\mathbf{m})$ and the likelihood $f(\mathbf{d}|\mathbf{m})$.

$$f(\mathbf{m}|\mathbf{d}) = \frac{f(\mathbf{d}|\mathbf{m})f(\mathbf{m})}{f(\mathbf{d})}, \tag{6}$$

where $f(\mathbf{d})$ is a normalization factor, called evidence. Assuming the forward modeling (Eq. (4)) as linear and under Gaussian assumptions, the MAP of the model parameters is given by (Emerick and Reynolds, 2013):

$$\mathbf{m}_{\text{MAP}} = \mu_{\text{m}} + \mathbf{K}(\mathbf{d} - \mathbf{G}\mu_{\text{m}}), \tag{7}$$

where μ_{m} is the mean of the prior distribution, **G** is the forward mapping operator, and **K** is the Kalman gain. The Kalman gain matrix relates the covariances of the model and data. We will further analyze its terms. For more details on ES-MDA derivation from the Bayes' rule and the Kalman filter, see Emerick and Reynolds (2013) and Liu and Grana (2018).

However, the MAP of the model parameters obtained utilizing the Kalman filter is intractable for nonlinear and high-dimensional. The ensemble-based methods are adopted to overcome this challenge. The ES-MDA method approximates the covariance model

with the empirical covariance of the ensemble members (Emerick and Reynolds, 2013). In ES-MDA, the posterior distribution is updated using the following equation:

$$\mathbf{m}_i^u = \mathbf{m}_i^p + \mathbf{K}\left(\mathbf{dobs}_i - \mathbf{d}_i^p\right), \tag{8}$$

for $i = 1, ..., N_e$ with N_e denoting the ensemble number, where the superscript u and p represent the posterior and prior distributions of the model variable $\mathbf{m}$, respectively, and $\mathbf{dobs}_i$ is the vector of observed data. The matrix $\mathbf{K}$ denotes the Kalman gain estimated from ensemble members given by

$$\mathbf{K} = \mathbf{C}_{md}^p \left(\mathbf{C}_{dd}^p + \alpha_j \mathbf{C_d}\right)^{-1}, \tag{9}$$

where $\mathbf{C}_{md}^p$ is the cross-covariance matrix between the prior vector of model parameters $\mathbf{m}^p$ and the vector of modeled data $\mathbf{d}^p$. The matrix $\mathbf{C}_{dd}^p$ is the auto-covariance matrix of predicted data, $\mathbf{C_d}$ is the covariance matrix of observed data measurement errors, and α_j is the inflation coefficient with $\alpha_j > 1$. Since the matrices $\mathbf{C}_{md}^p$ and $\mathbf{C}_{dd}^p$ cannot be analytically computed due to the nonlinearity of the forward operator, an approximation of these matrices is made using the empirical covariance from the ensemble members, given by, respectively,

$$\mathbf{C}_{md}^p = \frac{1}{N_e - 1} \sum_{i=1}^{N_e} \left(\mathbf{m}_i^p - \overline{\mathbf{m}}^p\right)\left(\mathbf{d}_i^p - \overline{\mathbf{d}}^p\right)^T, \tag{10}$$

and

$$\mathbf{C}_{dd}^p = \frac{1}{N_e - 1} \sum_{i=1}^{N_e} \left(\mathbf{d}_i^p - \overline{\mathbf{d}}^p\right)\left(\mathbf{d}_i^p - \overline{\mathbf{d}}^p\right)^T, \tag{11}$$

where $\overline{\mathbf{m}}^p = \sum_{i=1}^{N_e} \mathbf{m}_i^p$ and $\overline{\mathbf{d}}^p = \sum_{i=1}^{N_e} \mathbf{d}_i^p$.

Ensemble smoother performs a single full-step Gauss-Newton iteration for data assimilation. In ES-MDA, updating the ensemble of prior models iteratively is equivalent to performing multiple smaller corrections in the ensemble instead of a single and large Gauss-Newton correction (Emerick and Reynolds, 2013; Liu and Grana, 2018). In this approach, the posterior ensembles from one assimilation serve as prior ensembles for the next, with the same data being assimilated multiple times. Emerick and Reynolds (2012) proved the equivalence between the single and multiple steps in the linear-Gaussian scenario for the ensemble Kalman filter and evidenced that multiple steps can improve the estimates in the nonlinear scenario. The ES-MDA algorithm updates each ensemble to minimize the difference between the modeled and observed data. Therefore, the results are multiple models that honor the measurement and can be explored statistically.

As $\mathbf{C}_{dd}^p$ is a real-symmetric positive semi-definite matrix, $\mathbf{C} = \left(\mathbf{C}_{dd}^p + \alpha_j \mathbf{C_d}\right)^{-1}$ will also be real-symmetric positive-definite matrix if $\mathbf{C_d}$ is positive-definite (Emerick and Reynolds, 2013). However, Evensen (1994) highlights that the matrix $\mathbf{C}$ can be ill-posed, which leads to instability in the inverse problem. Therefore, Emerick and Reynolds (2013) argue that it is typical to use the Moore-Penrose' pseudoinverse when the number of measurements does not exceed the number of ensembles. In these cases, it is possible to bring stability to the inverse problem and maintain enough energy of the singular values.

For example, the behavior of acoustic impedance distribution before and after ten assimilations in the ES-MDA algorithm is shown in Fig. 1. After data assimilation, the mean of posterior

distribution converges to the true acoustic impedance value at a chosen well depth. The convergence does not occur to the exact value due to several factors, such as the noisy nature of seismic data and its limited frequency band. In addition, to the convergence between the modeled and observed values, a reduction in the standard deviation of the posterior distribution occurs when compared to the prior.

3.2. Bayesian classification

Bayes' theorem is a fundamental statistical approach to updating the probability of an event given some evidence. It shows how the *a priori* knowledge can change the *a posteriori* probability of a certain event. Bayesian classification is an application of Bayes' theorem for estimating the probability that a pattern of variables is related to a certain class. It assumes that the relevant probability values are known and that the decision problem is posed in probabilistic terms (Duda et al., 2001). Considering the class as a facies $\mathbf{y}_i$ and an elastic parameter $\mathbf{x}$, the Bayesian classification computes the *a posteriori* probability as follows:

$$P(\mathbf{y}_i|\mathbf{x}) = \frac{f(\mathbf{x}|\mathbf{y}_i)P(\mathbf{y}_i)}{f(\mathbf{x})}, \tag{12}$$

where $\mathbf{y}_i = 1, ..., n$ with $n = $ number of facies, $\mathbf{x}$ is the elastic parameter value, $f(\mathbf{x}|\mathbf{y}_i)$ is the likelihood function of the elastic parameter given the facies $\mathbf{y}_i$, $P(\mathbf{y}_i)$ is the *a priori* probability of $\mathbf{y}_i$, and $f(\mathbf{x})$ is the normalization function. The product of the likelihood function and the *a priori* probability is the most relevant part of Eq. (12), whereas the normalization factor just scales the *a posteriori* probabilities of all facies to sum one. Thus, this raises some special cases for the classification problem. Let $f(\mathbf{x}|\mathbf{y}_1) = f(\mathbf{x}|\mathbf{y}_2)$, then the observations give no clue about the occurrence of facies, consequently, the decision is given by the *a priori* probability. Also, if $P(\mathbf{y}_1) = P(\mathbf{y}_2)$, the facies are equally probable and the decision is entirely influenced by the likelihood functions. Hence, both factors are relevant for the Bayesian classification.

In this research, the classes of Bayesian facies classification are the facies. Facies is a geologic term used to distinguish rock bodies into mappable units based on physical characteristics, composition, formation, or other aspects (Gressly, 1838). Thus, the facies can be defined as lithofacies, petrofacies, electrofacies, flow units, or any other so that the choice is made based on the one that can enhance the reservoir characterization or has the best response to the well-log data of the study area. Authors such as Teixeira et al. (2017) and Penna et al. (2019) performed the Bayesian classification of lithofacies in the presalt interval, while Penna and Lupinacci (2021) and Lebre et al. (2021) used flow units.

The definition of the likelihood probability density function (PDF) of the facies is a crucial step in the Bayesian classification. It is done by assuming that the PDF f is unspecified, but only a dataset $\mathbf{x}$, which are samples of an unknown distribution. By this way, an approximation of the PDF is made using density estimation. The estimation can be performed parametrically or nonparametrically. The parametric approach is the case where the mean and variance parameters are used for defining the PDF by assuming the shape of the PDF. In non-parametric approaches such as kernel density estimation (KDE), no assumptions are made about the shape of data distribution. Herewith, the probability density function f tends to provide best fits to the distribution of the data in comparison to parametric PDFs. The PDF estimated through KDE is given by summing the individual kernel contribution of each sample according to the equation (Silverman, 1986):
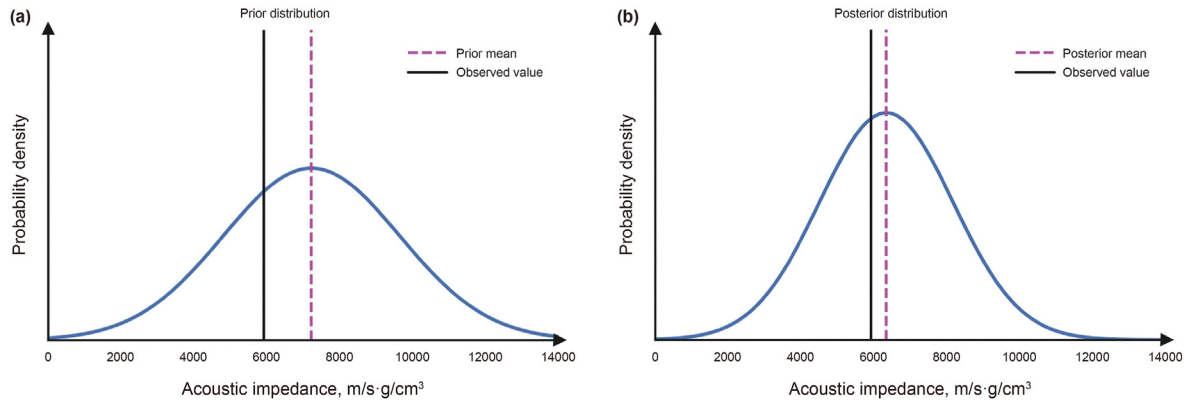
Fig. 1. Example of data assimilation performed in ES-MDA algorithm: **(a)** observed acoustic impedance value, prior distribution, and the mean of prior distribution before data assimilations; **(b)** observed acoustic impedance value, posterior distribution, and the mean of posterior distribution after ten data assimilations.

$$\widehat{f}(\mathbf{x}) = \frac{1}{nh} \sum_{i=1}^{n} \tilde{\mathbf{K}}\left(\frac{\mathbf{x} - \mathbf{x}_i}{h}\right), \tag{13}$$

where n is the number of samples in the dataset, the kernel type $\tilde{\mathbf{K}}$ determines the shape of the distribution, $\mathbf{x}_i$ is a sample from the dataset, and the bandwidth h inserts the width of the distribution window.

3.3. Porosity modeling

Porosity is a petrophysical property that plays a key role in petroleum exploration and production. Jointly with other properties like clay volume and water saturation, porosity estimation is mandatory to evaluate the presence of reservoirs and define the occurrence of commercial volumes of hydrocarbon. In the well-log scale, porosity is commonly estimated using conventional approaches based on the sonic, neutron, density, or their combination (Ellis and Singer, 2007). In the presalt carbonate reservoirs, Castro and Lupinacci (2022) observed a better fit of the porosities from the nuclear magnetic resonance (NMR) logs with laboratory data than those conventional methods mentioned.

Rock physics studies the relations between petrophysical properties, such as porosity, mineral fractions, and fluid saturations, and elastic properties, such as elastic moduli, velocities, density, and impedances (Mavko et al., 2009). These petro-elastic relations linking petrophysical properties to elastic attributes are widely used in reservoir characterization studies since elastic attributes are estimated from seismic data through seismic inversion (Grana et al., 2021). Thus, these relations allow an integration of information from different scales to generate 3D volumes of petrophysical properties. The process of porosity estimation from a seismic-inverted elastic parameter is called rock-physics inversion (Grana et al., 2022).

Empirical models are simple rock-physics relations to establish the connection between rock and fluid properties and elastic parameters and perform the rock-physics inversion. They are approximated by taking the shape of a function and determining its coefficients from the calibration of a regression to a dataset (Avseth et al., 2005). The relationship between the elastic and petrophysical properties depends on the purpose and available dataset. Some authors propose a linear relation between porosity and P-wave travel time (Wyllie et al., 1956), while others resort to a quadratic function (Raymer et al., 1980). Furthermore, the porosity can linearly relate to compressional velocity if the clay content remains significantly constant (Han et al., 1986). In presalt reservoirs, a lithological-dependent quadratic relationship is suitable for relating the acoustic impedance and effective porosity (Penna and Lupinacci, 2021).

Among the empirical models, two ways to perform the linear regression between properties are through the regressions using the L1 and L2 norms. The L2 norm, also known as the least-squares solution, is one in which the cost function is given by the square of the difference between the observed and the calculated data. In this type of solution, the minimization is done on the mean of absolute error and assumes that the data errors are independent and normally distributed. However, it can be strongly compromised by the presence of outliers in the dataset. To circumvent this problem, the L1 norm solution is preferable. In this case, the minimization is performed in norm 1 of the residual vector, and it is assumed that the errors in the data are distributed according to the Laplace distribution. The cost function of the solution using the L1 norm is given by (Aster et al., 2004):

$$\mu^{(1)} = \sum_{i=1}^{n} \frac{\left|\mathbf{d}_i - (\mathbf{Gm})_i\right|}{\sigma_i} = \|\mathbf{d}_{\mathrm{w}} - \mathbf{G}_{\mathrm{w}}\mathbf{m}\|_1, \tag{14}$$

where $\mathbf{d}_{\mathrm{w}}$ is the observed data, $\mathbf{G}_{\mathrm{w}}$ is the mapping operator, and $\mathbf{m}$ are the model parameters.

4. Methodology

We applied the workflow illustrated in Fig. 2 in the presalt interval. We evaluated the characterization of the coquina bank in the Well A area, while in the Well B area, we analyzed the extension and thickness of an igneous intrusion.

The interpretation of the main seismic horizons and the seismic-to-well tie were important to build the low-frequency model with a horizon-guided interpolation and for the wavelet estimation. The low-frequency model handles the lack of low-frequency content in the seismic amplitude altering from a relative acoustic impedance to an absolute one (Veeken and Da Silva, 2004).

4.1. Stochastic seismic inversion

We performed the stochastic seismic inversion using ES-MDA (Liu and Grana, 2018). The algorithm of ES-MDA consists of the following steps.

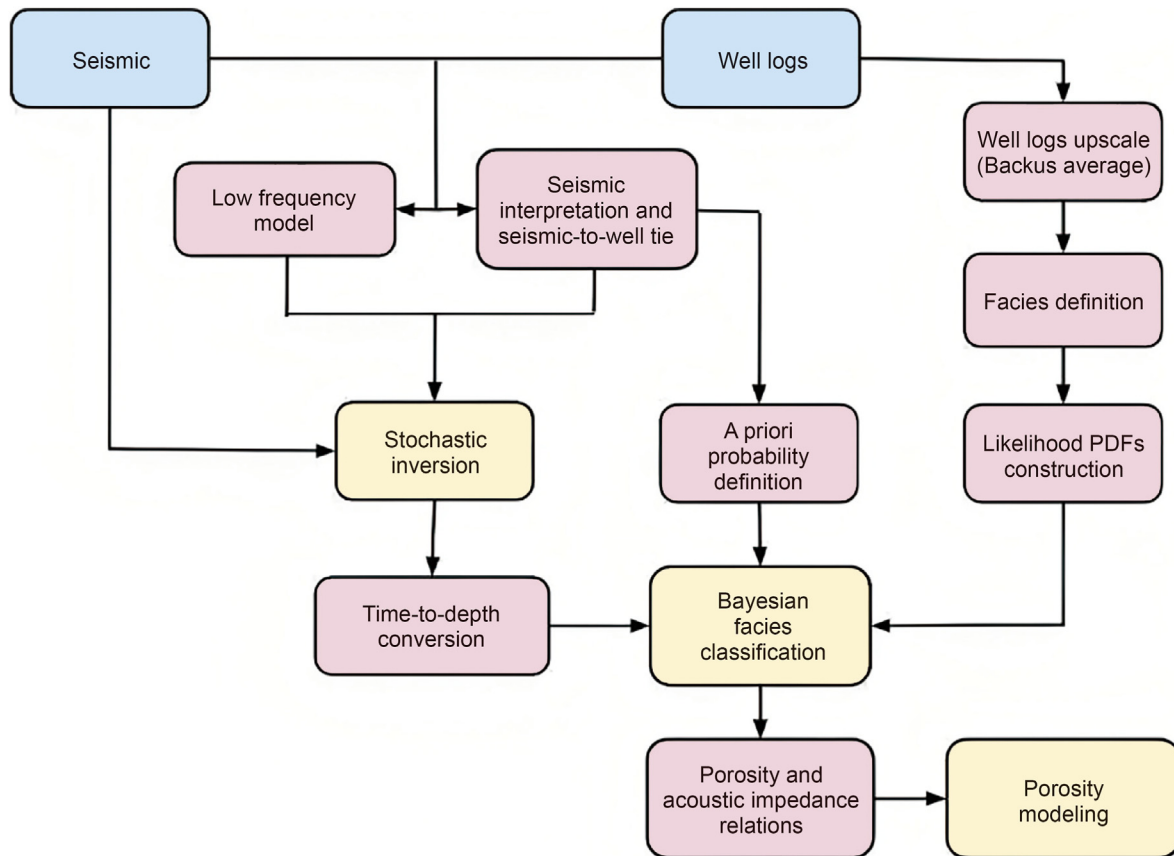1) Read seismic data, low-frequency model, and wavelet in the time domain.

Fig. 2. Workflow applied to stochastic inversion, Bayesian facies classification, and porosity modeling. The blue boxes represent the observed data, the pink boxes are the construction steps to the objective, and the yellow boxes are the main three steps performed.

2) Generation of acoustic impedance prior ensemble members for trace **x** and their forward modeling. For each trace **x**, we build vertical-correlated stochastic simulations (Doyen, 2007; Dvorkin et al., 2014; Fernandes and Lupinacci, 2021).

3) Application of ES-MDA algorithm (Eq. (8)), where the inverse of the matrix $\mathbf{C} = \left(\mathbf{C}_{dd}^{p} + \alpha_j \mathbf{C_d}\right)^{-1}$ is calculated using Moore-Penrose' pseudoinverse since the ensemble number is greater than measurements number for trace **x**.

4) After N_a assimilations, we calculate the posterior distribution statistics of parameters conditioned by seismic data.

We achieved the construction of the acoustic impedance simulations by imposing a vertical correlation between the values using a vertical correlation function. In the simulations, vertically close random values are similar, and as the distance increases, these values tend to lose their correlation. The vertical correlation function allows us to represent this behavior mathematically. This method aims to simulate a vertical geological continuity that is described by a variogram model (Dvorkin et al., 2014; Fernandes and Lupinacci, 2021).

We used an exponential theoretical variogram model with a range of 20 ms to build the vertical correlation function. The variogram model brings the high-frequency content to the stochastic realizations (Doyen, 2007). We set the number of simulations at 500. Then, we performed the forward modeling of simulations to obtain the predicted input data for ES-MDA for each trace. Within ES-MDA, the inputs are assimilated N_e times to fit the modeled data to the predicted data. In the example illustrated in Fig. 3, the input stochastic simulations of the algorithm for one trace are shown. A

low-frequency trend is observed in the input simulations associated with the low-frequency model extracted at the trace position. In addition to this trend, the variogram introduces a high frequency to the prior ensemble members. After the last assimilation, the forward modeling of the mean of acoustic impedance distribution converges fittingly to the observed data while the prior ensemble members are updated.

By repeating this process for all traces, statistical parameters from the posterior distribution of each of them are analyzed. We have chosen to work with the realizations equivalent to the percentiles P10, P50, and P90. Thus, we were able to evaluate an optimistic scenario (P10), a base one (P50), and a pessimistic one (P90). It is noteworthy that the terms optimistic and pessimistic used here assume that the highest acoustic impedance values are associated with lower porosities and vice versa. However, this relationship is not as straightforward for complex reservoirs as the presalt carbonates due to some non-reservoir facies like clayey rocks that present low acoustic impedance and porosity. This behavior highlights the reason to classify facies before modeling the porosity in our workflow.

4.2. Bayesian facies classification

For Bayesian classification, we upscaled the elastic parameter logs using Backus averaging (Backus, 1962) with a frequency of 100 Hz and 5-m sampling. We defined five facies, four of which were based on cutoffs of the effective porosity and clay volume logs using well-log data. The clay volume was estimated using Larionov' empirical model for old rocks (Larionov, 1969), and the effective
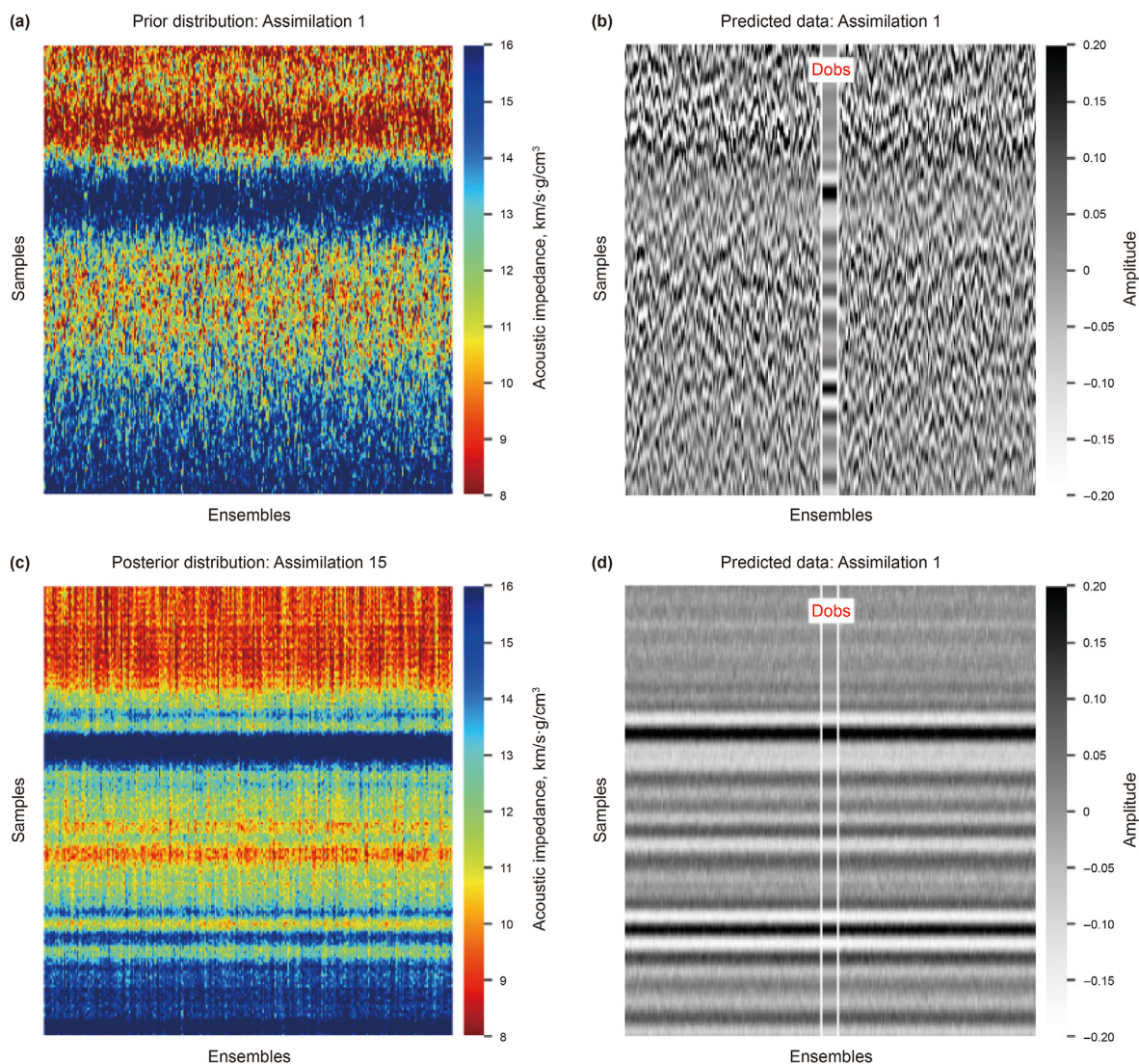
Fig. 3. Example of data assimilation in ES-MDA at one seismic trace: **(a)** prior ensemble members before the first assimilation; **(b)** forward modeling of **(a)**; **(c)** posterior ensemble members after the fifteenth and last assimilation; **(d)** forward modeling of **(c)**. The observed data (Dobs) is illustrated as a density plot in **(c)** and **(d)**.

porosity is from the NMR log. We used the information from well logs and composite log to define the intervals with the occurrence of igneous rocks. In igneous intervals with break-ups, the porosity was estimated using the sonic log (Ellis and Singer, 2007). The facies are high-porosity reservoirs (reservoir 1), intermediate-porosity reservoirs (reservoir 2), low-porosity carbonates (tight carbonates), clayey, and igneous rocks. Table 1 shows the criteria for defining these five facies. Reservoirs 1 and 2 are considered the reservoir intervals, while tight carbonates, clayey rocks, and igneous rocks are non-reservoirs.

Table 1
Criteria for defining the facies using well-logs data and composite profile, where φ_e is the effective porosity and V_{clay} is the clay volume.

Facies	Cutoffs
Reservoir 1	$\varphi_e > 12\%$ and $V_{clay} < 20\%$
Reservoir 2	$6\% \leq \varphi_e \leq 12\%$ and $V_{clay} < 20\%$
Tight carbonates	$\varphi_e < 6\%$ and $V_{clay} < 20\%$
Clayey	$\varphi_e < 6\%$ and $V_{clay} > 20\%$
Igneous	Well logs and composite profile

We built the likelihood PDFs through KDE using the upscaled acoustic impedance (IP) logs from well logs separately for the Barra Velha and Itapema Formations (Fig. 4). For kernel bandwidth estimation, we used Scott' method with a Gaussian-type kernel (Scott, 1992).

In the Itapema Formation, the igneous rocks present in the wells are extrusive. At the lowest IP values, there is a large overlap between reservoir 1 and clayey intervals, which impairs the distinction of these two facies in Bayesian classification. The confusion matrices for both formations using an equal *a priori* probability (0.20 for each facies) are shown in Fig. 5. The estimation of the confusion matrix is part of the classification data-driven feasibility study, in which the same acoustic impedance data are used for the construction of the PDFs and the Bayesian classification.

The accuracies in the Barra Velha and Itapema Formations are 55% and 67%, respectively. There is a good hit rate for reservoirs 1 in the Barra Velha Formation, while in the Itapema Formation, both reservoirs 1 and 2 have a hit rate higher than 70%. However, there are some uncertainties in the Barra Velha Formation caused by the overlap between PDFs, as is the case of clayey intervals and reservoirs 2, with 33.7% of reservoir 2 classified as clayey rocks, and
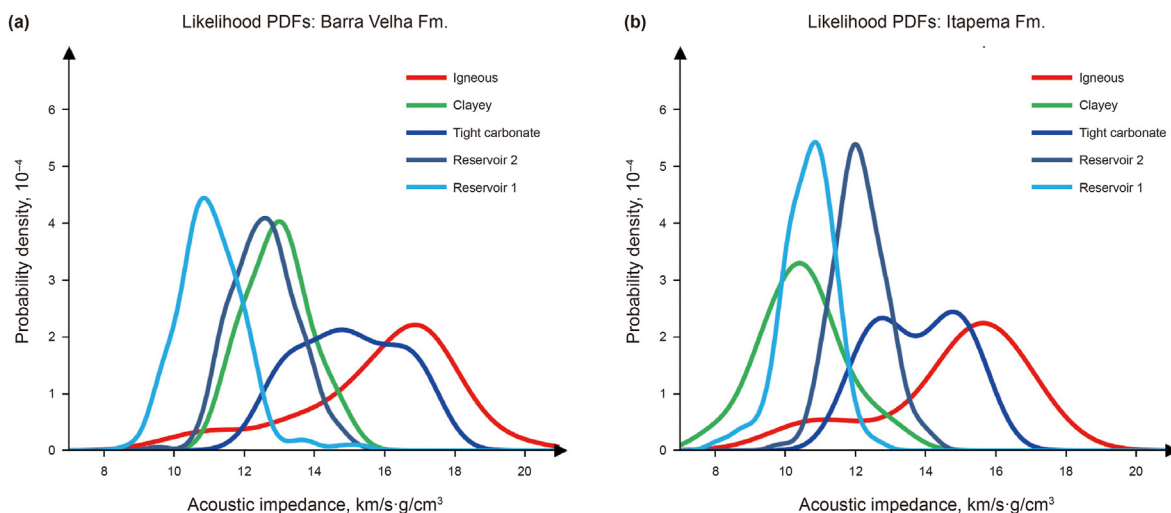
(a)

(b)

Fig. 4. Likelihood PDFs of acoustic impedance values for the five facies defined in the **(a)** Barra Velha Formation (Fm.) and **(b)** Itapema Formation.
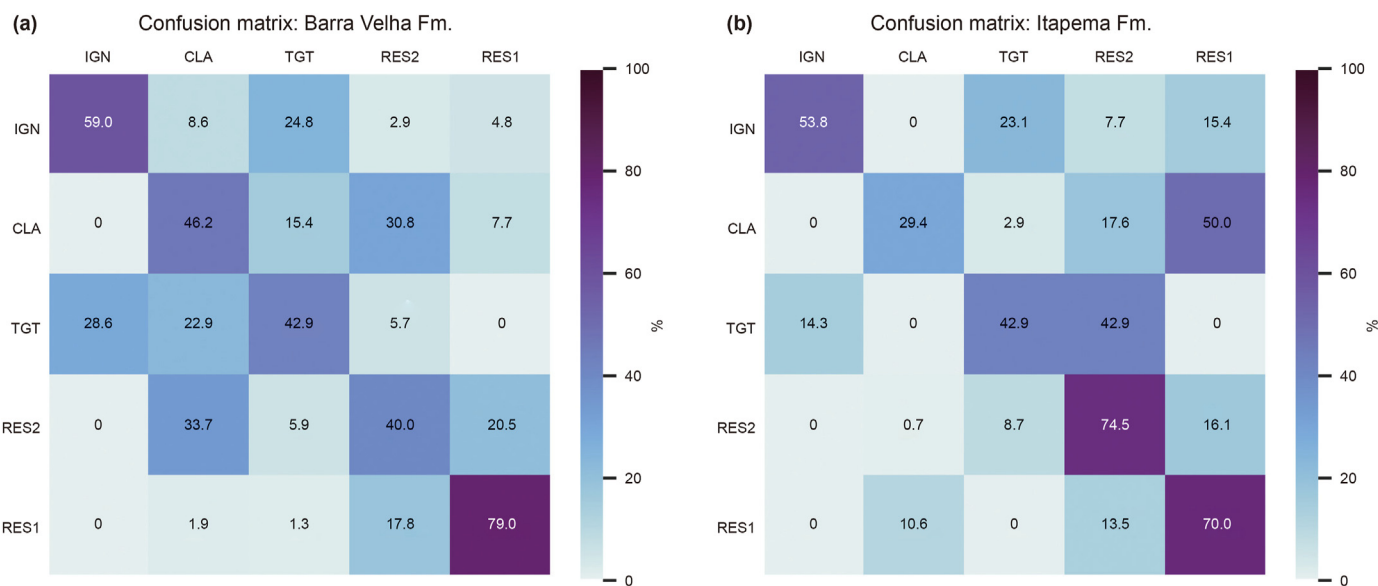
(a)

(b)

Fig. 5. Confusion matrices between facies in the **(a)** Barra Velha Formation and **(b)** Itapema Formation. The matrix rows indicate the observed facies, and the columns are the classified facies. The facies are the igneous rocks (IGN), clayey rocks (CLA), tight carbonates (TGT), reservoir 2 (RES2), and reservoir 1 (RES1).

igneous and tight carbonates, where 24.8% of igneous rocks were inferred as tight carbonates. In the Itapema Formation, the hit rate of the clayey facies is the lowest, with a 50% uncertainty with reservoir 1. Therefore, the identification of clayey rocks and their distinction from reservoirs is impaired in both formations.

Projects in oil and gas companies drilled wells on the structural highs of presalt reservoirs, which allegedly are the best geological targets. Thus, the well positions induce a bias in the likelihood PDFs, which can lead to incorrect predictions (Gonzalez et al., 2016). Depositional models for presalt consider that clayey intervals are associated with the structural lows, while the structural highs are dominated by clean carbonates (Wright and Barnett, 2015; Chinelatto et al., 2020). One way to incorporate this information into Bayesian classification is through the *a priori* probability. The approach where *a priori* probability of each facies is equal to 0.2 is very simple and is inconsistent with the geological setting, resulting in the overlap in reservoirs and clayey intervals, as previously seen in Fig. 5. Since there is no evidence of an expressive

structural inversion in the study area, we chose to introduce a geological knowledge into the Bayesian classification by modifying the *a priori* probability of the clayey facies and the reservoirs based on the depth of the Pre-Jiquiá and Pre-Alagoas Unconformities (Fig. 6). By holding the *a priori* probability of igneous rocks and tight
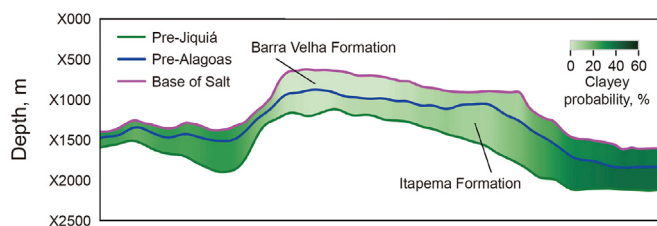

Fig. 6. Schematic seismic section illustrating the clayey rocks *a priori* probability approach applied to introduce prior geological knowledge in the Bayesian classification algorithm.

carbonates equal to 0.2 for each, we perform a balance between the clayey rocks and reservoir 1 and 2, totalizing 0.6 of probability. At the deepest parts of the Pre-Jiquiá and Pre-Alagoas Unconformities (structural lows of the Itapema and Barra Velha Formations, respectively), the *a priori* probability of the clayey facies dominates over that of the reservoirs: 0.6 for clayey rocks, 0 for reservoir 2, and 0 for reservoir 1. At the shallowest parts of both unconformities (structural highs), the *a priori* probability of the reservoirs will overcome that of clayey rocks: 0.3 for reservoir 2, 0.3 for reservoir 1, and 0 for clayey rocks.

4.3. Porosity modeling

After the Bayesian facies classification, we performed the porosity modeling using the acoustic impedance and the most probable facies volumes from the realizations equivalent to the percentiles P10, P50, and P90. For this modeling, we used the L1-norm linear fits to the effective porosity and acoustic impedance relationships for the upscaled well-logs data. The effective porosity log used is from NMR logs in non-igneous zones and the sonic log in igneous intervals. We chose the L1 norm due to the presence of outliers in the dataset since it is more unaffected by spurious points than the L2 norm. We established five equations for each formation, one for reservoir 1, reservoir 2, tight carbonates, and igneous rocks, while in clayey intervals, the porosity was set as zero (Fig. 7).

We decided to fit a linear function for the four facies due to its linear behavior observed in the individual plots. In addition, using five relations at each formation catches the full potential of the classified facies. By joining two or more facies with one relation—for example, reservoir 1, reservoir 2, and tight carbonates—their separation in the Bayesian classification step would become unneeded and mask the identification of the best porosity intervals. Despite the similar linear coefficient observed in reservoir 1 and reservoir 2, the different angular coefficient highlights different trends on each facies in both formations. Concerning the tight carbonates, they cover very distinguishing processes for their generation, like contact metamorphism, silicification, and dolomitization. Thus, disregarding the clayey rocks, this facies presents the highest dispersion and worst fit correlation in both formations. Joining the tight carbonates with other facies would worsen the modeling step. The uncertainties in the porosity model are analyzed by performing the porosity modeling in the percentiles P10 and P90 of acoustic impedance and their respective modeled facies using the same equations shown in Fig. 7.

5. Results

The metrics used for quantitatively evaluating seismic inversion were the correlation coefficient and the mean absolute percentage error (*MAPE*). The correlation coefficient indicates how the estimated variable is linearly correlated with the observed variable. On the other hand, a lower *MAPE* indicates how dispersed the estimated variable is from the observed variable. These two metrics also are adopted for evaluating the porosity modeling. Quantitatively, the seismic inversion reached satisfactory results in Wells A and B, as shown in Table 2. The comparisons were performed with the observed upscaled log and the acoustic impedance trace extracted at well position in the time domain. A correlation coefficient of 0.93, as calculated in Well B, can be considered excellent for the low seismic resolution and high geological complexity of the presalt reservoirs. The correlation coefficient and *MAPE* estimated in Well A are also adequate to carry out the Bayesian classification without high uncertainties associated with inverted acoustic impedance.

The results of stochastic acoustic inversion, Bayesian

classification, and porosity modeling on a seismic section crossing Well A are presented in Fig. 8. The main target of this well was a coquina bank in the Itapema Formation, which developed in a drowning regime with continuous generation of accommodation space (Neves et al., 2019; Oliveira et al., 2021). The upper interval of the Itapema Formation is marked by low/medium IP values, with an excellent correlation with the upscaled IP from the well log. In this interval, the best reservoirs were classified, with high confidence given by probabilities higher than 70% and with the porosity modeling reaching values of approximately 20%. The yellow/orange tones in the porosity model represent values close to the 15% porosity average estimated by Carlotto et al. (2017) for a well drilled in a presalt coquina bank. Seismic inversion was also able to recover the high IP values associated with the tight carbonates in the lower interval of Well A, with porosities of less than 6%. In this zone, the Bayesian classification was unable to identify thin reservoir 1 layers. This difficulty is associated with the vertical resolution of the inversion result. Indeed, the reservoir 1 probability is smaller than 20% in these thin layers. The result is also good in the Barra Velha Formation, with its lower interval marked by high porosity values near Well A, with an opposite behavior to that observed in the Itapema Formation, presenting a porosity decrease towards the top. The porosity model identifies a reservoir 1 body with intermediate porosity (14–18%) in a mounded-like feature in the structurally higher portion of the Barra Velha Formation (8000–9000 m), constituting a potential reservoir target. The workflow performed satisfactorily for estimating the well behavior of the increase in porosity towards the upper interval Itapema Formation. In the structural low (0–2000 m), our approach estimated an intercalation between clayey rocks and tight carbonates, with the former associated with the low/intermediate acoustic impedance values and the second associated with the high values. It is mainly marked by zero-to-low porosity zones consisting of a non-reservoir interval.

Quantitatively, the Bayesian classification reached good results in Well A. Fig. 9 illustrates the confusion matrix between observed and classified facies at Well A position and the crossplot between observed and estimated porosity from the P50 of acoustic impedance and facies using the linear-equations fits. The Bayesian classification accuracy estimated is 63.4%. The correlation coefficient for porosity is close to that for inversion, indicating a good relationship between acoustic impedance, facies, and porosity in the interval near Well A. The porosity modeling in reservoir 1 intervals is excellent at the highest porosities (greater than 14%), while the results are underestimated at intermediate porosities (greater than 12% and lower than 14%). The reservoir 1 samples with underestimated porosity caused a significant increase in *MAPE*, reaching 27.4%. The main uncertainty estimated is between tight carbonates and reservoir 2. The PDFs overlap causes this and is an expected behavior given that these two facies are lithologically similar, differing only by the cutoff of 6% set in the porosity log. At the tight carbonate intervals that were classified as reservoir 2, the porosity is overestimated. The opposite behavior is also expected due to the 32.6% of reservoir 2 being classified as tight carbonates. Our approach adopted in the *a priori* probability for Bayesian facies classification assisted in the non-identification of clayey intervals in the coquina bank.

The uncertainties associated with porosity modeling were estimated based on the realizations equivalent to the percentiles P10 and P90 for the optimistic and pessimistic scenarios (Fig. 10). The P10 facies presents misclassified clayey rocks below the Pre-Alagoas Unconformity caused by the estimate of low inverted IP values (7–8 km/s·g/cm³), in an IP range that the ponderation of *a priori* probability in the structural high was not able to contour the control of the clayey rocks in the likelihood PDFs. This resulted in a
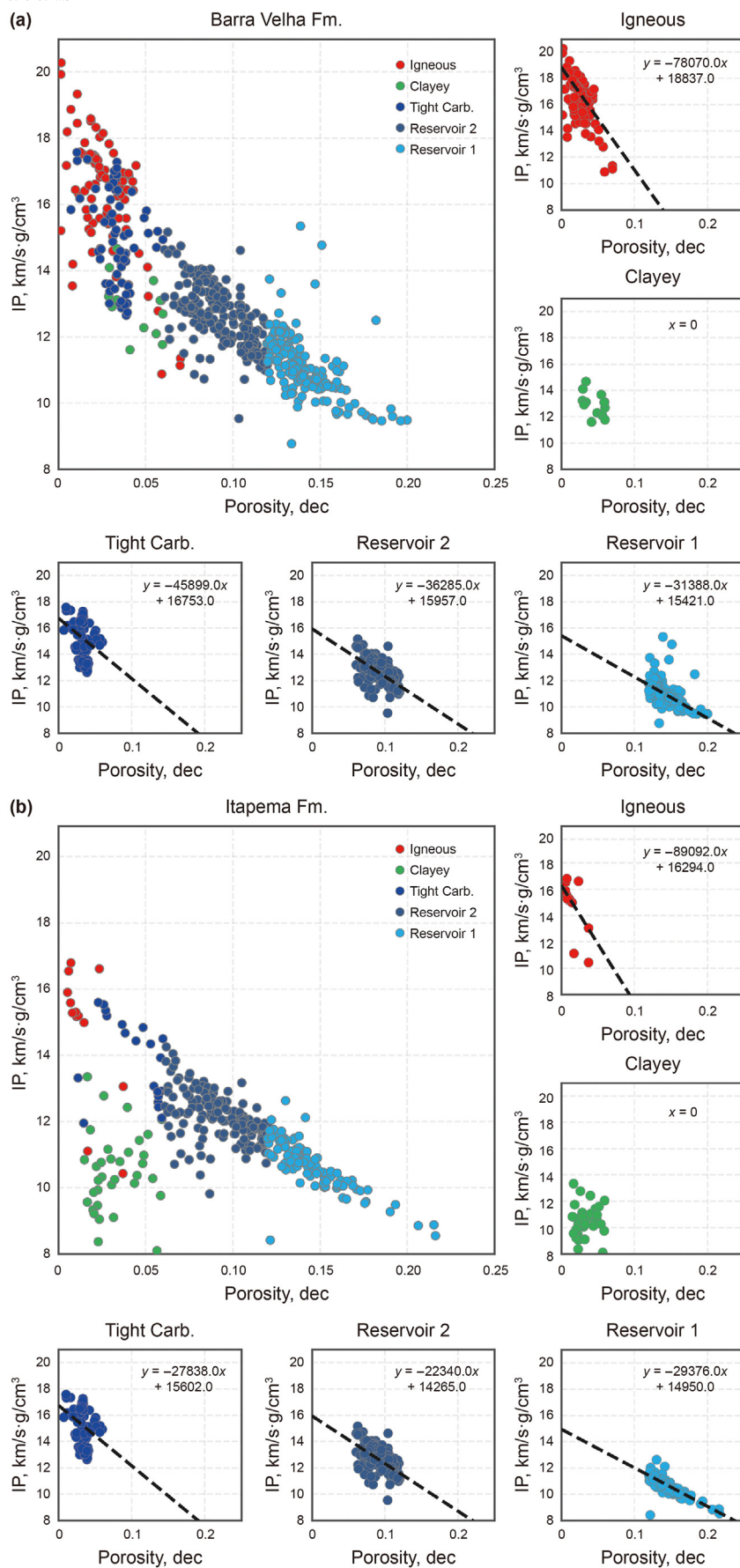
Fig. 7. Linear-equations fits of porosity and IP performed using the L1 norm for reservoirs 1 and 2, tight carbonates (Carb.), and igneous rocks from data from nine wells in the **(a)** Barra Velha Formation and **(b)** Itapema Formation.

Table 2
Correlation coefficient and mean absolute percentage error (*MAPE*) estimated in Wells A and B.

Well	Correlation coefficient, %	*MAPE*, %
A	73.0	8.48
B	93.6	6.61

strong decay in the porosity estimate from P10. On the other hand, the P90 estimated false probabilities of igneous rocks near the top and the bottom of the well. Elsewhere, we notice that the observed porosity values are coherent with the estimate in the well, setting between P10 and P90 with a high correlation with the three re-alizations equivalent to the percentiles.

We evaluate the capability of the stochastic inversion and Bayesian classification for identifying the igneous rocks extension in the west-east seismic section crossing Well B (Fig. 11). The igneous rock is a diabase intrusion that occurred near the carbonate-salt interface, in the upper interval of the Barra Velha Formation. Identifying the extension and thickness of these igneous bodies is challenging and ambiguous using the seismic amplitude only. In the base scenario (P50), the thickness of the igneous rock is in excellent visual agreement with the one observed in Well B. This occurred due to the capability of the stochastic acoustic inversion of recovering the high IP values characteristics of the igneous rocks in this interval, being this well the one that reached the highest cor-relation coefficient calculated. A thinning of the intrusion is observed in the dip direction (range from 0 to 2000 m). Further-more, in the P10 and P50 scenarios, there is a near-to-zero proba-bility of igneous rocks in the interval 4000–6000 m. In the P90 scenario, this region is marked by probabilities lower than 50%.

In the P10 scenario, the probabilities of igneous rocks greater than 20% are observed at 500–4000 m, while values greater than 50% are estimated in the neighborhood of Well B. In the P90 sce-nario, these probabilities reach values between 20% and 50% in the 4000–6000 m range. However, these estimates are greater than 50% in 0–4000 m, indicating that even in the pessimistic scenarios, the behavior of the igneous distribution remains similar, with a higher probability between 0 and 4000 m. Therefore, the percentile analysis ratifies the comportment observed in the P50 scenario. Table 3 summarizes the igneous hit rate, classified thickness, and its extension for the realizations equivalent to the three percentiles.

Our result in the P50 vol ratifies the analysis of the visual agreement between observed and classified facies, with an esti-mated thickness of 90 m, which is close to the observed thickness in Well B. Despite the higher hit rate in P90, the thickness of the igneous rock was overestimated in this scenario, with 53.8% of the tight carbonates classified as igneous. On the other hand, P10 underestimated the igneous thickness, presenting igneous intervals classified as tight carbonates. This uncertainty between tight car-bonates and igneous rock is expected during the identification of these facies in the Bayesian classification. In the three scenarios, the highest probability of igneous rock occurs in the neighborhood of Well B.

6. Discussion

Since the presalt discovery, different workflows have been adopted for the quantitative seismic interpretation and character-ization of the presalt reservoirs. Several of them use seismic inversion (Teixeira et al., 2017; Dias et al., 2019; Peçanha et al., 2019; Penna et al., 2019; Barnett et al., 2021; Ferreira et al., 2021; Penna and Lupinacci, 2021). The use of ES-MDA for stochastic seismic inversion is relatively recent, with Liu and Grana (2018) being the
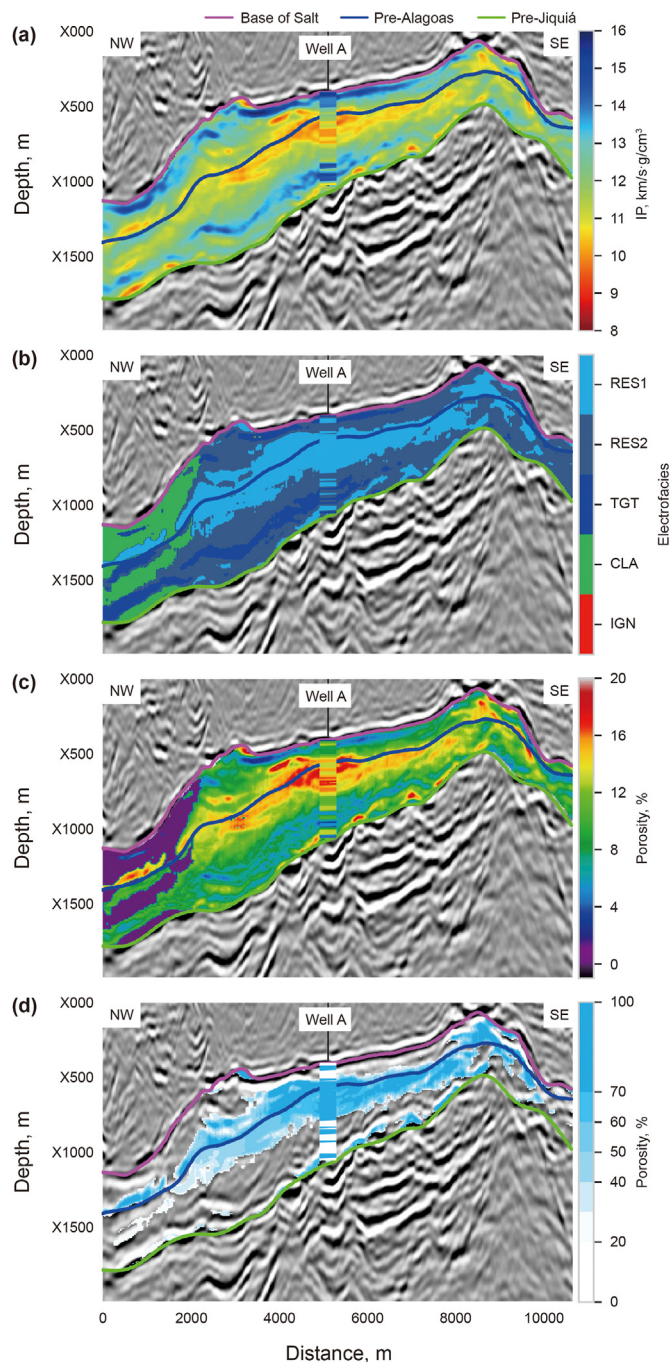

Fig. 8. Seismic section that crosses the Well A, with **(a)** IP (P50) from stochastic inversion, **(b)** classified facies from Bayesian classification, **(c)** porosity model, and **(d)** reservoir 1 facies probability. In all items, the lime green line is the Pre-Jiquiá Un-conformity, the blue line is the Pre-Alagoas Unconformity, and the magenta line is the Base of Salt. Seismic data is courtesy of CGG.

first to explore this method for this purpose. The success of its applications in presalt shows that the ES-MDA is a robust method also for geologically-complex datasets with low vertical seismic resolution. ES-MDA handles the nonlinearity of the forward model for the largest angles of the Zoeppritz equations in elastic inversion. In our application, we did not utilize the maximum potential of the method, as we employed it for acoustic inversion. Nevertheless, its reasonably simple implementation and efficient computational cost encouraged us to apply the ES-MDA in our presalt dataset, and
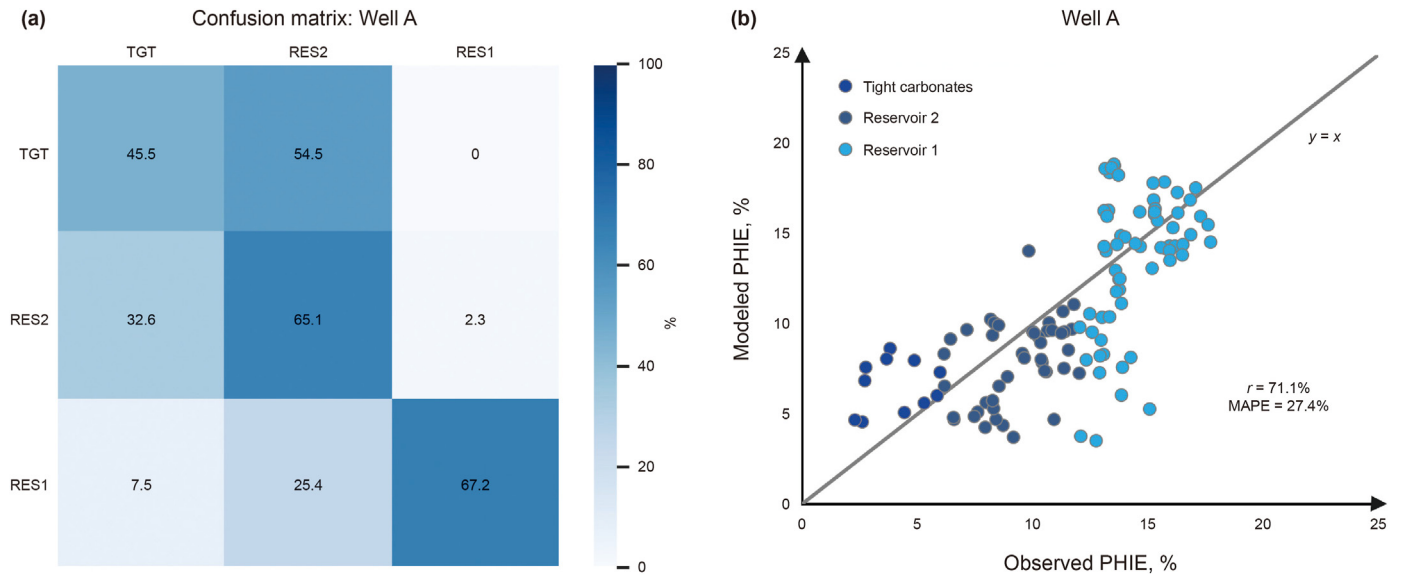
Fig. 9. Quantitative evaluation of Bayesian classification and porosity modeling in Well A, showing **(a)** the confusion matrix and **(b)** the crossplot of observed porosity versus estimated porosity colored by the observed facies, with the correlation coefficient (*r*) and the mean absolute percentage error (*MAPE*).
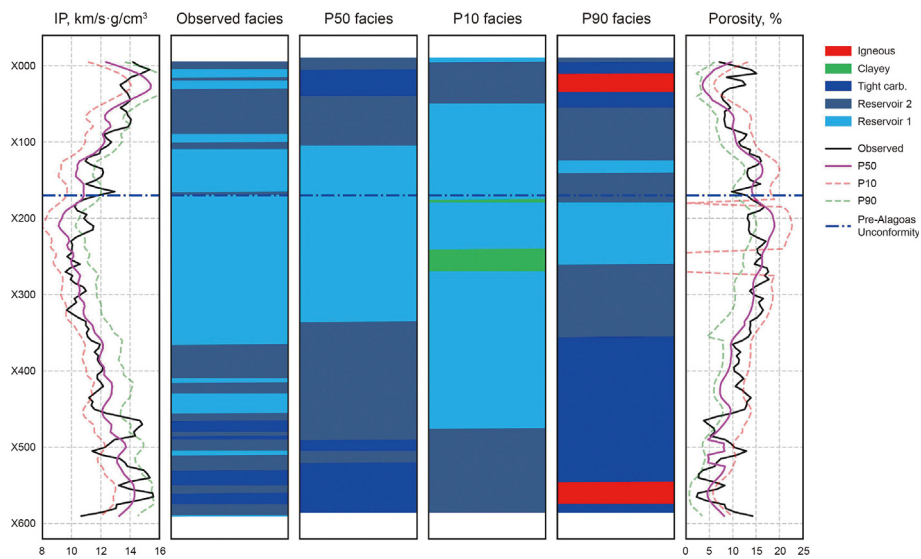

Fig. 10. IP, classified facies, and modeled porosity of the percentiles P10, P50, and P90 extracted at Well A position.

the results show that the algorithm fits well for the purpose.

A very important input in stochastic inversion using ES-MDA is the prior ensemble members. We used an approach for its generation based on constructing spatially correlated stochastic simulations in time (Doyen, 2007; Dvorkin et al., 2014). Therefore, our input simulations do not have horizontal correlation, so it was not possible to use unique and selected simulations because the behavior becomes completely non-geologic due to poor lateral continuity. The alternative we chose was using the realizations equivalent to the percentiles P10, P50, and P90, which proved suitable for our approach. However, Liu and Grana (2018) point out that other simulation-generation methods, such as variogram-based and multiple-point geostatistics algorithms, can be integrated with ES-MDA. Thus, the selection of specific simulations after data assimilations is possible. Liu and Grana (2019) use the FFT-moving average and probability field simulation for generating the prior ensemble members for stochastic simulations. This

method stands out for its computational efficiency in large grids (Simm and Bacon, 2014; Liu and Grana, 2019) when compared to variogram-based approaches such as sequential Gaussian simulation (Doyen, 2007) because it does not require the construction of the local PDF at every grid cell to incorporate previously simulated samples.

Also, within ES-MDA, the proposal presented by Liu and Grana (2018) allows for a joint seismic and rock-physics inversion. However, we believe that this strategy is not suitable for a presalt dataset due to the multimodal behavior of porosity and acoustic impedance (previously shown in Fig. 8). The use of a single rock-physics model, for example, calibrated for clay-poor carbonates, tends to significantly overestimate porosity values in non-reservoir intervals, such as the clayey facies. In this aspect, the Bayesian facies classification works on inferring a facies before modeling porosity. The distinction between clay-poor and clay-rich facies is a requisite for porosity estimation since rock-physics models for the presalt
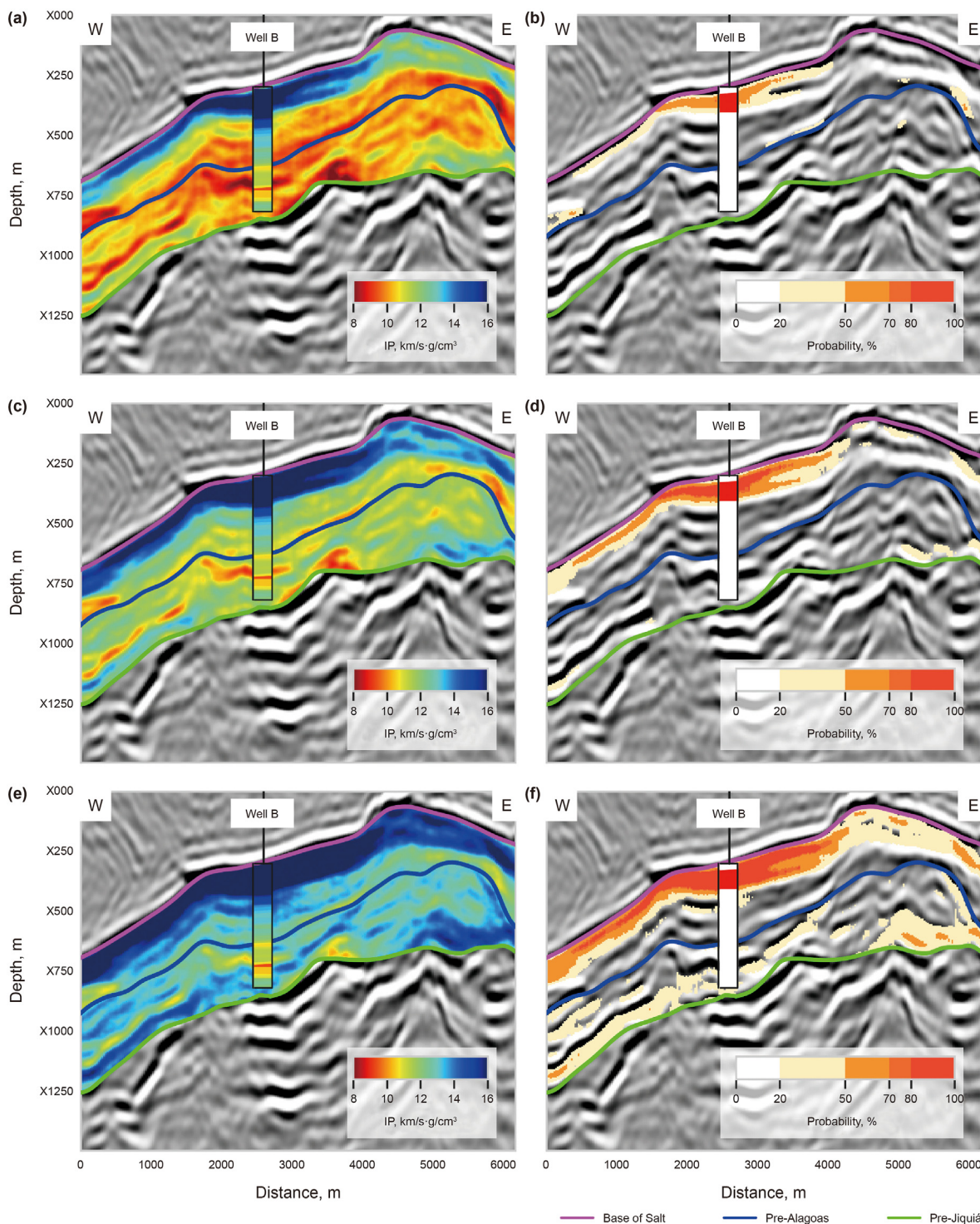
Fig. 11. Seismic section crossing Well B showing the IP of stochastic inversion from the realizations equivalent to the percentiles **(a)** P10, **(c)** P50, and **(e)** P90 and their respective igneous occurrence probability estimated in Bayesian classification: **(b)** igneous probability from P10; **(d)** igneous probability from P50; **(f)** Igneous probability from P90. The lime green line represents the Pre-Jiquiá Unconformity, the blue line is the Pre-Alagoas Unconformity, and the magenta line is the Base of Salt. Seismic data is courtesy of CGG.

rocks highlight that clay minerals and calcite, dolomite, and quartz contents modify the trend on the acoustic impedance and porosity domain (Vasquez et al., 2019; Mello and Lupinacci, 2022). In our work, in addition to clay minerals and variations in mineralogical content, the presence of igneous rocks is a factor that brings more difficulty in fitting a unique rock-physics model.

Due to the introduction of geological knowledge in the *a priori*

probability, the facies model is accurate in both formations. This strategy proved necessary to reduce the bias caused by the well position. Teixeira et al. (2017) used an *a priori* probability model with the same strategy we adopted to solve the overlap between porous and clayey carbonates. For their case, they used the elastic parameters IP versus VP/VS (ratio between P-wave velocity and S-wave velocity) in the Bayesian classification and successfully

Table 3
Hit rate and estimated thickness extracted at Well B position and W-E extension of igneous facies estimated in the realizations equivalent to the percentiles P10, P50, and P90. The igneous rock thickness observed in the well data is 85 m.

	P10	P50	P90
Igneous hit rate	64.7%	94.1%	100%
Estimated thickness	55 m	90 m	115 m
W-E extension	2000 m	3700 m	4500 m

modeled the facies in a presalt dataset, exemplifying a well drilled in the structural low, which was dominated by shaley carbonates with approximately 100% of shaley carbonates *a posteriori* probability. Here, the classification becomes more critical because we used only IP. However, we consider the results satisfactory using only IP, with the facies accurately identified on the coquina bank at Well A and the non-identification of clayey rocks on the structural highs. In addition, this approach proved effective for predicting scenarios for the igneous rock extension in Well B.

The comparison between the Bayesian facies classification with the *a priori* probability ponderation and with the equal *a priori* probability for the five facies (Fig. 12) underlines the improvement in consistency of the facies model with our proposed method. The traditionally equal approach presents clayey rocks over the structurally higher area, predominantly in the Barra Velha Formation. These areas were classified as reservoir 2 in the proposed approach. As introduced in the model, we expect that clean carbonates dominate these areas, while structural lows are dominated by clayey facies associated with low-energy deposits (Wright and Barnett, 2015). In the traditional approach, an inaccurate clayey interval was classified near Well A in the upper part of the Itapema Formation in a reservoir 1 zone, causing a decrease from 63.4% to 53.7% in the prediction accuracy. These two differences—reservoir 1 and clayey rocks in the Itapema Formation and reservoir 2 and clayey rocks in the Barra Velha Formation—emerged from facies with great overlaps between PDFs, demonstrating the capability of the *a priori* probability in improving the results qualitatively and quantitatively by imposing a geological knowledge. Non-reservoir facies prevail in the structural low (0–2000 m), with the alternation of clayey rocks and tight carbonates (Fig. 12(a)), while the clean facies propagate to the lows in Fig. 12(b). This inconsistent model overestimates the reservoir zones in the field.

We successfully characterized the coquina bank of the Itapema Formation applying the proposed approach. Coquina banks are important exploratory targets of many fields in the presalt, so a large number of studies deal with the depositional and diagenetic processes that acted on these rocks (Carlotto et al., 2017; Pietzsch et al., 2018; Barnett et al., 2021; Oliveira et al., 2021). Generally,

the coquina bank exhibits a backstepping pattern throughout its evolution (Oliveira et al., 2021). Barnett et al. (2021) show a seismic section in the presalt of the Santos Basin after elastic inversion, in which the authors identified the upper part of the coquina bank with lower acoustic and shear impedances than the lower part. They associate this upper interval with the best reservoirs. Our results corroborate the behavior highlighted by Barnett et al. (2021), with the upper interval of the coquina bank showing low acoustic impedance values, reservoir 1 facies, and porosity reaching 20% near Well A.

The magmatic events in the presalt may have been strongly influenced by faults. These faults, which suffered posterior reactivation, are important in the distribution of the intrusive igneous rocks of the Santonian-Campanian and Eocene magmatic events (Zhao et al., 2019). The delineation of intrusive igneous bodies in the presalt is not straightforwardly interpreted using only seismic amplitude. Intrusive igneous rocks present positive reflections, characterized by dikes and sills, saucer-shaped or bowl-shaped. Sills commonly occur in the presence of faults and may function in reactivating and vertically segmenting them (Omosanya et al., 2016). Intrusive igneous rocks tend to present high acoustic impedance, and this parameter supports its identification (Penna et al., 2019; Ren et al., 2019). Our approach enabled the generation of three models based on the generated scenarios to understand the extension of an intruded igneous rock at the carbonate-salt interface and its relationship to the presence of faults (Fig. 13).

The thickness of the igneous rock thins away from Fault F1, supporting the geological interpretation that this fault serves as a conduit for this intrusive layer. The three scenarios in Fig. 13 also suggest the propagation of the intrusive layer towards the structural low at the west of Fault F1. When the magmatic event found contrasting rock mechanical properties between carbonate-salt unconformity, it flows downwards from the top of Fault F1 into the relatively low-density surrounding carbonates in a gravity-driven movement. Outcrops provide examples of sills emplaced along unconformities (Mudge, 1968; Walker, 1989). Thus, understanding the spatial arrangement of the igneous rocks in presalt is substantial, as Penna et al. (2019) mention that these rocks can serve as a fluid flow barrier in the injection and production phases. Because of their significance, other recent studies propose different methodologies to identify these igneous rocks on seismic volume (Penna et al., 2019; Vizeu et al., 2021).

7. Conclusions

We presented a three-step approach that employs quantitative seismic interpretation routines for the porosity modeling of the
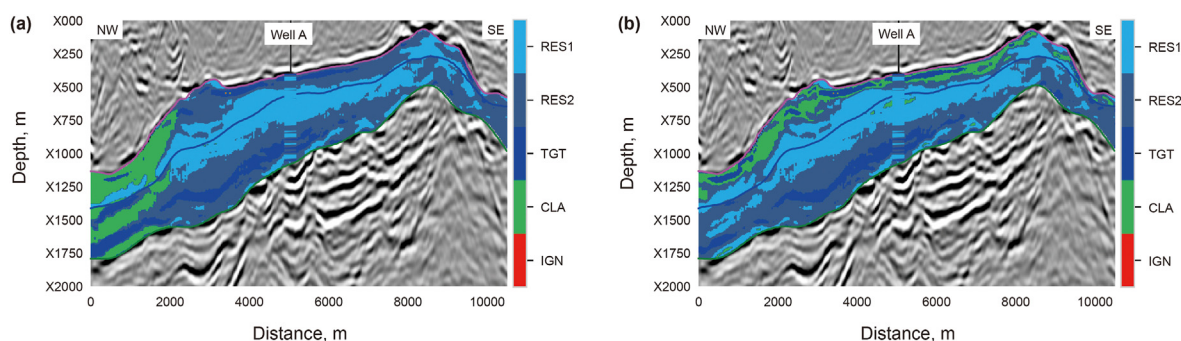

Fig. 12. Comparison between classified facies using **(a)** the proposed approach that relates the clayey *a priori* probability with the depth of Pre-Jiquiá and Pre-Alagoas Unconformities and **(b)** the traditional approach (all facies equally probable). The green line represents the Pre-Jiquiá Unconformity, the blue line is the Pre-Alagoas Unconformity, and the magenta line is the Base of Salt. Seismic data is courtesy of CGG.
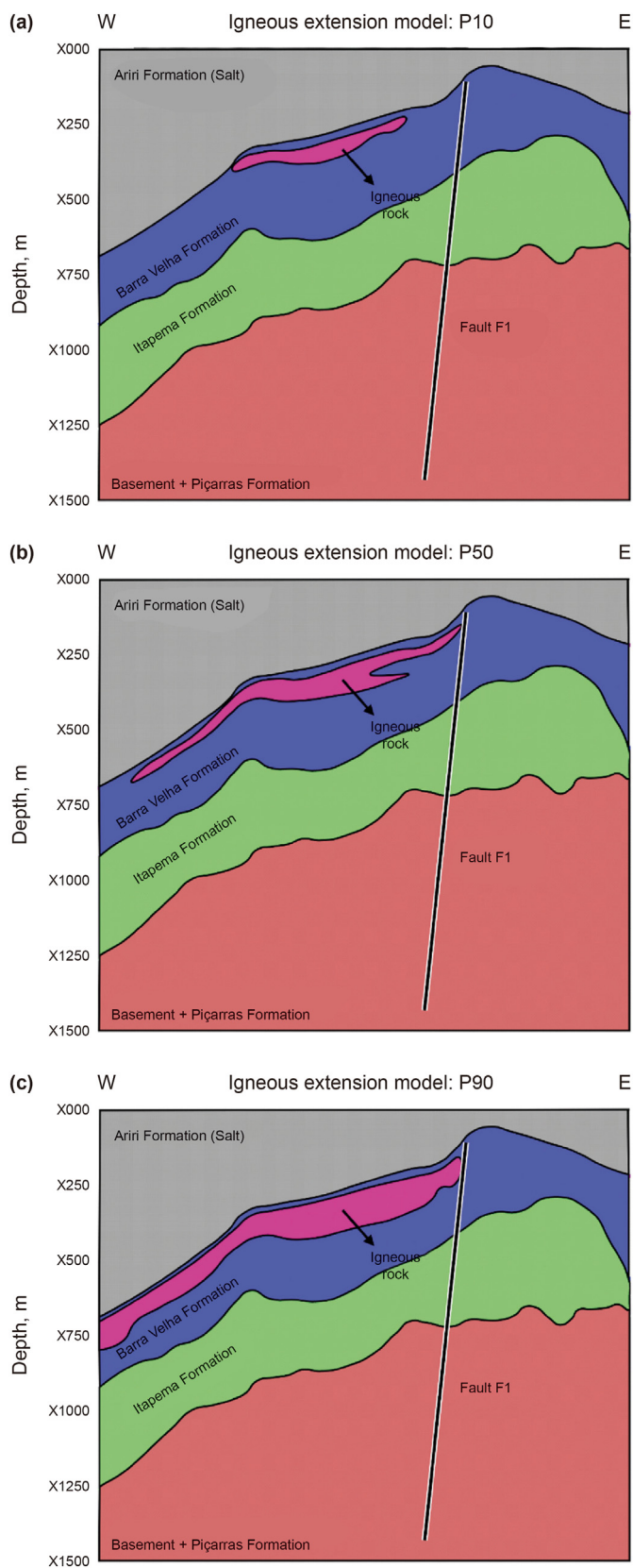
Fig. 13. Schematic models defined from realizations equivalent to the percentiles P10, P50, and P90 for the extension of the igneous intrusion that occurred in the carbonate-salt interface.

Brazilian presalt carbonate reservoirs and mapping the igneous intrusion extension and thickness. To accomplish this, we used the realizations equivalent to the percentiles P10, P50, and P90 from ES-MDA stochastic acoustic inversion for Bayesian facies classification. After, we derived the porosity modeling using empirical linear relations between effective porosity and acoustic impedance. ES-MDA works effectively for stochastic acoustic inversion in a geologically complex setting such as the presalt interval. The *a priori* probability of clayey facies ponderation proposed in the Bayesian facies classification was able to limit the occurrence of clayey rocks to structural lows, enabling a good characterization of the coquina bank. Using acoustic impedance constrained by facies for porosity modeling was crucial to overcoming the challenge of multimodality in the distributions of acoustic impedance and porosity. We estimated that the best porosities are in the upper interval of the coquina bank, with values reaching 20% near Well A, while low-porosity zones and tight carbonates mark the lower part. The correlation coefficient between observed and estimated porosities is 0.71, which influences the accuracy of the Bayesian classification of 0.63, illustrating a good result for the presalt scenario. The Bayesian classification was also crucial to understanding the spatial distribution of an igneous rock occurring in the carbonate-salt interface. In the percentile P50, the igneous facies hit rate is 0.94, indicating an excellent thickness estimation of this facies, with an extension of approximately 3700 m in the west-east direction. A thinning aspect is observed in the igneous intrusion in the dip direction, denoting an increase in the distance from the source conduit.

Declaration of competing interest

The authors declare that they have no known competing financial interests or personal relationships that could have appeared to influence the work reported in this paper.

Acknowledgments

References

Aki, K., Richards, P.G., 1980. Quantitative Seismology: Theory and Methods. Freeman, San Francisco, CA.

Allo, F., Coulon, J.P., Formento, J.L., Reboul, R., Capar, L., Darnet, M., Issautier, B., Marc, S., Stopin, A., 2021. Characterization of a carbonate geothermal reservoir using rock-physics-guided deep neural networks. Lead. Edge 40 (10), 751–758. https://doi.org/10.1190/tle40100751.1.

ANP, 2022. Boletim da Produção de Petróleo e Gás Natural. Superintendência de Desenvolvimento e Produção 148, 41 (in Portuguese).

Aster, R.C., Borchers, B., Thurber, C., 2004. Parameter Estimation and Inverse Problems. Academic Press.

Avseth, P., Mukerji, T., Mavko, G., 2005. Quantitative Seismic Interpretation: Applying Rock Physics Tools to Reduce Interpretation Risk. Cambridge University Press.

Azevedo, L., Soares, A., 2017. Geostatistical methods for reservoir geophysics. Springer, Switzerland. https://doi.org/10.1007/978-3-319-53201-1.

Azevedo, L., Grana, D., Amaro, C., 2019. Geostatistical rock physics AVA inversion. Geophys. J. Int. 216 (3), 1728–1739. https://doi.org/10.1093/gji/ggy511.

Backus, G.E., 1962. Long-wave elastic anisotropy produced by horizontal layering. J. Geophys. Res. 67 (11), 4427–4440. https://doi.org/10.1029/JZ067i011p04427.

Barnett, A.J., Fu, L., Rapasi, T., Scotellaro, C., Guha, J., Cabolova, A., Domingues, A.L., 2021. Seismic characterization and origin of clinoforms in lacustrine depositional environments: a case study from the Cretaceous of the South Atlantic. Geol. Soc., London, Special Publications 509 (1), 127–145. https://doi.org/10.1144/SP509-2019-148.

Bhattacharya, S., 2021. A primer on machine learning in subsurface geosciences. SpringerBriefs in Petroleum Geoscience & Engineering 1, 1–172. https://doi.org/

10.1007/978-3-030-71768-1.

Bortoli, L.J., Alabert, F., Haas, A., Journel, A., 1993. Constraining stochastic images to seismic data. In: Geostatistics Tróia'92. Springer, Dordrecht, pp. 325–337. https://doi.org/10.1007/978-94-011-1739-5_27.

Braga, I., Barbosa, I., Puga, J., Franco, A., Pereira, L.D., Ouverney, G., 2019. Facies classification in 3d seismic data volume of the brazilian pre-salt through convolutional neural networks technology. In: Brazilian Geophysical Society, 16th International Congress of the Brazilian Geophysical Society & EXPOGEF. Rio de Janeiro, Brazil.

Buland, A., Omre, H., 2003. Bayesian linearized AVO inversion. Geophysics 68 (1), 185–198. https://doi.org/10.1190/1.1543206.

Canchumuni, S.W., Emerick, A.A., Pacheco, M.A.C., 2019. History matching geological facies models based on ensemble smoother and deep generative models. J. Pet. Sci. Eng. 177, 941–958. https://doi.org/10.1016/j.petrol.2019.02.037.

Carlotto, M.A., Silva, R.C.B., Yamato, A.A., Trindade, M.A., Moreira, J.L.P., Fernandes, R.A.R., Ribeiro, O.J.S., Gouveia Jr., W.P., Carminati, J.P., Qicai, D., Junfeng, Z., Silva-Telles Jr., A.C., 2017. Libra: A Newborn Giant in the Brazilian Presalt Province. AAPG Special Volumes. https://doi.org/10.1306/13572006M1133685.

Castro, T.M., Lupinacci, W.M., 2022. Comparison between conventional and NMR approaches for formation evaluation of presalt interval in the Buzios Field, Santos Basin, Brazil. J. Petrol. Sci. Eng. 208, 109679. https://doi.org/10.1016/j.petrol.2021.109679.

Chinelatto, G.F., Belila, A.M.P., Basso, M., Souza, J.P.P., Vidal, A.C., 2020. A taphofacies interpretation of shell concentrations and their relationship with petrophysics: a case study of Barremian-Aptian coquinas in the Itapema Formation, Santos Basin-Brazil. Mar. Petrol. Geol. 116, 104317. https://doi.org/10.1016/j.marpetgeo.2020.104317.

Connolly, P.A., Hughes, M.J., 2016. Stochastic inversion by matching to large numbers of pseudo-wells. Geophysics 81 (2), M7–M22. https://doi.org/10.1190/geo2015-0348.1.

Cunha, C.A., Damasceno, A., Pimentel, A.L., Teixeira, L.M.S., Cruz, N.M.S.M., Oliveira, T.A.S., 2019. High resolution impedance inversion. Braz. J. Genet. 37 (4), 461–469. https://doi.org/10.22564/rbgf.v37i4.2022.

Cyz, M., Azevedo, L., 2020. Direct geostatistical seismic amplitude versus angle inversion for shale rock properties. IEEE Trans. Geosci. Rem. Sens. 59 (6), 5335–5344. https://doi.org/10.1109/TGRS.2020.3017091.

Das, V., Pollack, A., Wollner, U., Mukerji, T., 2019. Convolutional neural network for seismic impedance inversion. Geophysics 84 (6), R869–R880. https://doi.org/10.1190/geo2018-0838.1.

Dias, R.M., Castro, T.M., Santos, M.A.C., Lupinacci, W.M., 2019. Understanding the relationship between acoustic impedance and porosity in the presalt of the Buzios Field, Santos Basin. In: First EAGE Workshop on Pre-Salt Reservoir: from Exploration to Production, 2019. European Association of Geoscientists & Engineers, pp. 1–5 (1). https://doi.org/10.3997/2214-4609.201982009.

Doyen, P., 2007. Seismic Reservoir Characterization: An Earth Modelling Perspective. EAGE Publication.

Duda, R.O., Hart, P.E., Stork, D., 2001. Pattern Classification. A Wiley-Interscience Publication.

Dvorkin, J., Gutierrez, M., Grana, D., 2014. Seismic Reflections of Rock Properties. Cambridge University Press, Cambridge.

Ellis, D.V., Singer, J.M., 2007. Well logging for earth scientists, Vol. 692. Springer, Dordrecht.

Emerick, A.A., Reynolds, A.C., 2012. History matching time-lapse seismic data using the ensemble Kalman filter with multiple data assimilations. Comput. Geosci. 16, 639–659. https://doi.org/10.1007/s10596-012-9275-5.

Emerick, A.A., Reynolds, A.C., 2013. Ensemble smoother with multiple data assimilation. Comput. Geosci. 55, 3–15. https://doi.org/10.1016/j.cageo.2012.03.011.

Evensen, G., 1994. Sequential data assimilation with a nonlinear quasi-geostrophic model using Monte Carlo methods to forecast error statistics. J. Geophys. Res.-Oceans 99 (C5), 10143–10162. https://doi.org/10.1029/94JC00572.

Fatti, J.L., Smith, G.C., Vail, P.J., Strauss, P.J., Levitt, P.R., 1994. Detection of gas in sandstone reservoirs using AVO analysis: a 3-D seismic case history using the Geostack technique. Geophysics 59 (9), 1362–1376. https://doi.org/10.1190/1.1443695.

Fernandes, F.J.D., Lupinacci, W.M., 2021. Pseudo-wells generation by spatial-correlated stochastic simulations. In: First SEG Latin America Virtual Student Conference, Society of Exploration Geophysicists.

Ferreira, D.J.A., Dias, R.M., Lupinacci, W.M., 2021. Seismic pattern classification integrated with permeability-porosity evaluation for reservoir characterization of presalt carbonates in the Buzios Field, Brazil. J. Pet. Sci. Eng. 201, 108441. https://doi.org/10.1016/j.petrol.2021.108441.

Gineste, M., Eidsvik, J., 2017. Seismic waveform inversion using the ensemble Kalman smoother. 79th EAGE Conference and Exhibition 2017 (1), 1–5. https://doi.org/10.3997/2214-4609.201700794. European Association of Geoscientists & Engineers.

Gineste, M., Eidsvik, J., Zheng, Y., 2020. Ensemble-based seismic inversion for a stratified medium. Geophysics 85 (1), R29–R39. https://doi.org/10.1190/geo2019-0017.1.

Gonzalez, E.F., Gesbert, S., Hofmann, R., 2016. Adding geologic prior knowledge to Bayesian lithofluid facies estimation from seismic data. Interpretation 4 (3), SL1–SL8. https://doi.org/10.1190/INT-2015-0220.1.

Grana, D., Della Rossa, E., 2010. Probabilistic petrophysical-properties estimation integrating statistical rock physics with seismic inversion. Geophysics 75 (3), O21–O37. https://doi.org/10.1190/1.3386676.

Grana, D., Mukerji, T., Dvorkin, J., Mavko, G., 2012. Stochastic inversion of facies from seismic data based on sequential simulations and probability perturbation method. Geophysics 77 (4), M53–M72. https://doi.org/10.1190/geo2011-0417.1.

Grana, D., Mukerji, T., Doyen, P., 2021. Seismic Reservoir Modeling: Theory, Examples, and Algorithms. John Wiley & Sons.

Grana, D., Azevedo, L., de Figueiredo, L., Connolly, P., Mukerji, T., 2022. Probabilistic inversion of seismic data for reservoir petrophysical characterization: review and examples. Geophysics 87 (5), 1–99. https://doi.org/10.1190/geo2021-0776.1.

Gressly, A., 1838. Observations géologiques sur le Jura Soleurois. auf Kosten der Gesellschaft (in French).

Han, D.H., Nur, A., Morgan, D., 1986. Effects of porosity and clay content on wave velocities in sandstones. Geophysics 51 (11), 2093–2107. https://doi.org/10.1190/1.1442062.

Herlinger, J.R.R., Zambonato, E.E., De Ros, L.F., 2017. Influence of diagenesis on the quality of Lower Cretaceous pre-salt lacustrine carbonate reservoirs from northern Campos Basin, offshore Brazil. J. Sediment. Res. 87 (12), 1285–1313. https://doi.org/10.2110/jsr.2017.70.

Jesus, C., Olho Azul, M., Lupinacci, W.M., Machado, L., 2019. Multiattribute framework analysis for the identification of carbonate mounds in the Brazilian presalt zone. Interpretation 7, T467–T476. https://doi.org/10.1190/INT-2018-0004.1.

Kalman, R.E., 1960. A new approach to linear filtering and prediction problems. ASME. J. Basic Eng. 82 (1), 35–45. https://doi.org/10.1115/1.3662552.

Ketteb, R., Djeddi, M., Kiche, Y., 2019. Modeling of porosity by geostatistical methods. Arabian J. Geosci. 12 (8), 268. https://doi.org/10.1007/s12517-019-4450-9.

Kolbjørnsen, O., Buland, A., Hauge, R., Røe, P., Ndingwan, A.O., Aker, E., 2020. Bayesian seismic inversion for stratigraphic horizon, lithology, and fluid prediction. Geophysics 85 (3), R207–R221. https://doi.org/10.1190/geo2019-0170.1.

Lang, X., Grana, D., 2017. Geostatistical inversion of prestack seismic data for the joint estimation of facies and impedances using stochastic sampling from Gaussian mixture posterior distributions. Geophysics 82 (4), M55–M65. https://doi.org/10.1190/geo2016-0670.1.

Larionov, V.V., 1969. Borehole Radiometry. Nedra, Moscow.

Latimer, R.B., 2011. Inversion and interpretation of impedance data. Interpretation of Three-Dimensional Seismic Data, pp. 309–350. https://doi.org/10.1190/1.9781560802884.ch9.

Lebre, M.B.S., Fernandes, F.J.D., Vizeu, F., Jesus, I.L., Freire, A.F.M., Gamboa, L.A.P., Lupinacci, W.M., 2021. Electrofacies versus flow units in presalt carbonate reservoirs of the Santos Basin: which is the best approach for estimate petrophysical properties?. In: 17th International Congress of the Brazilian Geophysical Society & EXPOGEF Rio de Janeiro, Brazil.

Liu, M., Grana, D., 2018. Stochastic nonlinear inversion of seismic data for the estimation of petroelastic properties using the ensemble smoother and data reparameterization. Geophysics 83 (3), M25–M39. https://doi.org/10.1190/geo2017-0713.1.

Liu, M., Grana, D., 2019. Accelerating geostatistical seismic inversion using TensorFlow: a heterogeneous distributed deep learning framework. Comput. Geosci. 124, 37–45. https://doi.org/10.1016/j.cageo.2018.12.007.

Mavko, G., Mukerji, T., Dvorkin, J., 2009. The Rock Physics Handbook: Tools for Seismic Analysis of Porous Media. Cambridge University Press.

Mello, V.L., Lupinacci, W.M., 2022. Mineralogy based classification of carbonate rocks using elastic parameters: a case study from Buzios Field. J. Pet. Sci. Eng., 109962 https://doi.org/10.1016/j.petrol.2021.109962.

Milani, E.J., Rangel, H.D., Bueno, G.V., Stica, J.M., Winter, W.R., Caixeta, J.M., Neto, O.P., 2007. Bacias sedimentares brasileiras: cartas estratigráficas. Bol. Geociencias Petrobras 15 (2), 183–205 (in Portuguese).

Moreira, J.L.P., Madeira, C.V., Gil, J.A., Machado, M.A.P., 2007. Bacia de Santos. Bol. Geociencias Petrobras 15 (2), 531–549 (in Portuguese).

Mudge, M.R., 1968. Depth control of some concordant intrusions. Geol. Soc. Am. Bull. 79 (3), 315–332.

Mukerji, T., Jørstad, A., Avseth, P., Mavko, G., Granli, J.R., 2001. Mapping lithofacies and pore-fluid probabilities in a North Sea reservoir: seismic inversions and statistical rock physics. Geophysics 66 (4), 988–1001. https://doi.org/10.1190/1.1487078.

Neves, I.A., Lupinacci, W.M., Ferreira, D.J.A., Zambrini, J.P.R., Oliveira, L.O.A., Olho Azul, M., Ferrari, A.L., 2019. Presalt reservoirs of the Santos Basin: cyclicity, electrofacies, and tectonic-sedimentary evolution. Interpretation 7 (4), SH33–SH43. https://doi.org/10.1190/INT-2018-0237.1.

Oliveira, F.V.C.S.R.S., Gomes, R.T.M., Silva, K.M.S., 2019. Log features for the characterization of igneous rocks in the pre-salt area of Santos Basin, SE Brazil. In: International Conference & Exhibition (ICE), Buenos Aires, Argentina, 27-30 August 2019, 11264. American Association of Petroleum Geologists (AAPG).

Oliveira, L., Pimentel, F., Peiro, M., Amaral, P., Christovan, J., 2018. A seismic reservoir characterization and porosity estimation workflow to support geological model update: pre-salt reservoir case study, Brazil. First Break 36 (9), 75–85. https://doi.org/10.3997/1365-2397.n0122.

Oliveira, L., Rancan, C.C., Sartorato, A.C.L., Farias, F.A., Pereira, E., 2021. Drowning unconformities on presalt carbonate platforms—examples from the Itapema Formation (lower cretaceous), Santos Basin, offshore Brazil. Palaeogeogr. Palaeoclimatol. Palaeoecol. 577, 110570. https://doi.org/10.1016/j.palaeo.2021.110570.

Omosanya, K.O., Harishidayat, D., Johansen, S.E., 2016. Seismic interpretation and characterization of igneous rocks in jan mayen microcontinent, Norwegian-Greenland sea. In: Society of Exploration Geophysicists and American Association of Petroleum Geologists, pp. 149–149. https://doi.org/10.1190/ice2016-

6257477.1.

Peçanha, A.A., Lupinacci, W.M., Ferreira, D.J.A., Freire, A.F.M., 2019. A workflow for reservoir characterization applied to presalt coquinas from the Linguado Field, Campos Basin, Brazil. J. Pet. Sci. Eng. 183, 106451. https://doi.org/10.1016/j.petrol.2019.106451.

Penna, R., Araújo, S., Geisslinger, A., Sansonowski, R., Oliveira, L., Rosseto, J., Matos, M., 2019. Carbonate and igneous rock characterization through reprocessing, FWI imaging, and elastic inversion of a legacy seismic data set in Brazilian presalt province. Lead. Edge 38 (1), 11–19. https://doi.org/10.1190/tle38010011.1.

Penna, R., Lupinacci, W.M., 2021. 3D modelling of flow units and petrophysical properties in brazilian presalt carbonate. Mar. Petrol. Geol. 124, 104829. https://doi.org/10.1016/j.marpetgeo.2020.104829.

Pietzsch, R., Oliveira, D.M., Tadeschi, L.R., Neto, J.V.Q., Figueiredo, M.F., Vazquez, J.C., Souza, R.S., 2018. Palaeohydrology of the Lower Cretaceous pre-salt lacustrine system, from rift to post-rift phase, Santos Basin, Brazil. Palaeogeogr. Palaeoclimatol. Palaeoecol. 507, 60–80. https://doi.org/10.1016/j.palaeo.2018.06.043.

Russell, B.H., 1988. Introduction to Seismic Inversion Methods (No. 2). SEG Books.

Raymer, L.L., Hunt, E.R., Gardner, J.S., 1980. An improved sonic transit time-to-porosity transform. In: SPWLA 21st Annual Logging Symposium. OnePetro.

Ren, K., Oliveira, M.J.R., Zhao, J., Zhao, J., Oliveira, L.C., Rancan, C.C., Carmo, I.O., Deng, Q., 2019. Using wireline logging and thin sections to identify igneous contact metamorphism and hydrothermal influence on presalt limestone reservoirs in Libra Block, Santos Basin. In: Offshore Technology Conference Brasil. OnePetro. https://doi.org/10.4043/29818-MS.

Scott, D.W., 1992. Multivariate Density Estimation: Theory, Practice, and Visualization. John Wiley & Sons, New York, Chicester. https://doi.org/10.1002/9781118575574.

Shuey, R.T., 1985. A simplification of the Zoeppritz equations. Geophysics 50 (4), 609–614. https://doi.org/10.1190/1.1441936.

Silverman, B.W., 1986. Density Estimation for Statistics and Data Analysis, Vol. 26. CRC Press.

Simm, R., Bacon, M., 2014. Seismic Amplitude: an Interpreter's Handbook. Cambridge University Press.

Soares, A., Diet, J.D., Guerreiro, L., 2007. Stochastic inversion with a global perturbation method. In: EAGE Conference on Petroleum Geostatistics. European Association of Geoscientists & Engineers cp-32. https://doi.org/10.3997/2214-4609.201403048.

Stordal, A.S., 2015. Iterative Bayesian inversion with Gaussian mixtures: finite sample implementation and large sample asymptotics. Comput. Geosci. 19 (1), 1–15. https://doi.org/10.1007/s10596-014-9444-9.

Tarantola, A., 2005. Inverse Problem Theory and Methods for Model Parameter Estimation. Society for Industrial and Applied Mathematics. https://doi.org/10.1137/1.9780898717921.

Teixeira, L., Cruz, N., Silvany, P., Fonseca, J., 2017. Quantitative seismic interpretation integrated with well-test analysis in turbidite and pre-salt reservoirs. Lead. Edge 36 (11), 931–937. https://doi.org/10.1190/tle36110931.1.

Thurin, J., Brossier, R., Métivier, L., 2017. Ensemble-based uncertainty estimation in full waveform inversion. In: 79th Annual International Conference and Exhibition, EAGE, Extended Abstracts. https://doi.org/10.1093/gji/ggz384.

Vasquez, G.F., Morschbacher, M.J., dos Anjos, C.W.D., Silva, Y.M.P., Madrucci, V., Justen, J.C.R., 2019. Petroacoustics and composition of presalt rocks from Santos Basin. Lead. Edge 38 (5), 342–348. https://doi.org/10.1190/tle38050342.1.

Veeken, P.C.H., Da Silva, A.M., 2004. Seismic inversion methods and some of their constraints. First Break 22 (6). https://doi.org/10.3997/1365-2397.2004011.

Vizeu, F., Neto, E.R.O., Freire, A.F.M., Lupinacci, W.M., 2021. Convolutional neural network for prediction of igneous seismic facies in the Santos Basin pre-salt. Second EAGE Conference on Pre-Salt Reservoir 2021 (1), 1–5. https://doi.org/10.3997/2214-4609.202183008.

Wang, Y., 2016. Seismic Inversion: Theory and Applications. John Wiley & Sons.

Walker, G.P., 1989. Gravitational (density) controls on volcanism, magma chambers and intrusions. Aust. J. Earth Sci. 36 (2), 149–165. https://doi.org/10.1080/08120098908729479.

Wright, V.P., Barnett, A.J., 2015. An abiotic model for the development of textures in some South Atlantic early Cretaceous lacustrine carbonates. Geol. Soc., London, Special Publications 418 (1), 209–219. https://doi.org/10.1144/SP418.3.

Wright, V.P., Rodriguez, K., 2018. Reinterpreting the South Atlantic pre-salt 'microbialite' reservoirs: petrographic, isotopic and seismic evidence for a shallow evaporitic lake depositional model. First Break 36 (5), 71–77. https://doi.org/10.3997/1365-2397.n0094.

Wyllie, M.R.J., Gregory, A.R., Gardner, L.W., 1956. Elastic wave velocities in heterogeneous and porous media. Geophysics 21 (1), 41–70. https://doi.org/10.1190/1.1438217.

Zhao, J., Oliveira, M.J.R., Zhao, J., Ren, K., Oliveira, L.C., Carmo, I.O., Rancan, C.C., Deng, Q., 2019. Fault activity and its influences on distribution of igneous rocks in Libra Block, Santos Basin: semi-quantitative to quantitative assessment of fault activity based on high-resolution 3d seismic data. In: Offshore Technology Conference Brasil. OnePetro. https://doi.org/10.4043/29691-MS.